

## REVIEW

View Article Online  
View Journal | View IssueCite this: *Mater. Chem. Front.*,  
2024, 8, 1451Perovskite and layered perovskite oxynitrides for  
efficient sunlight-driven artificial synthesisJeongsuk Seo \*<sup>a</sup> and Kazunari Domen <sup>bc</sup>

Perovskite and layered perovskite oxynitrides are regarded as promising visible-light-responsive semiconductors for efficient artificial photosynthesis to produce renewable value-added energy resources, including H<sub>2</sub>, formic acid (HCOOH), and ammonia (NH<sub>3</sub>). This is because of their chemical stability in aqueous electrolytes at various pH values, along with a narrow bandgap and a suitable band position bestowing ideal optical properties. In this review, we discuss recent advances in photocatalysis using perovskite and layered perovskite oxynitrides responsive to a wide wavelength range of the visible-light spectrum. Next, we address in detail how the photoactivity of oxynitrides can be enhanced with respect to their synthesis, including bulk and surface engineering such as doping (or substitution), controlling their morphology, and crystal facet engineering. Finally, we discuss the existing challenges to realizing efficient artificial photosynthesis using these materials.

Received 18th September 2023,  
Accepted 4th December 2023

DOI: 10.1039/d3qm01019h

rsc.li/frontiers-materials

1. Perovskite and layered perovskite  
oxynitrides

Perovskite-type oxynitrides are mixed metallic compounds with the general formula AB(O,N)<sub>3</sub>, where A and B represent a large alkali-earth metal or La (*i.e.*, A = Ca, Sr, Ba, or La) and a relatively small transition metal (*i.e.*, B = Ti, Ta, or Nb), respectively.<sup>1–3</sup> The stoichiometry of anions O and N in the perovskite is determined by the combination of cations at the A and B sites. Fig. 1 displays the crystal structure of an ideal cubic

<sup>a</sup> Department of Chemistry, College of Natural Sciences, Chonnam National University, 77 Yongbong-ro, Buk-gu, Gwangju 61186, Republic of Korea.  
E-mail: j\_seo@chonnam.ac.kr

<sup>b</sup> Research Initiative for Supra-Materials, Shinshu University, 4-17-1 Wakasato, Nagano 380-8553, Japan

<sup>c</sup> Office of University Professors, The University of Tokyo, 2-11-16 Yayoi, Bunkyo-ku, Tokyo 113-8656, Japan



Jeongsuk Seo

Jeongsuk Seo is currently an associate professor in Department of Chemistry at Chonnam National University, Republic of Korea. She received her PhD degree under the supervision of Prof. Kazunari Domen in Chemical System Engineering from The University of Tokyo in 2014. Since then, she joined the Japan Technological Research Association of Artificial Photosynthetic Chemical Process (ARPCHEM) as a postdoctoral researcher. She moved to Shinshu

University as an assistant professor in 2017 and then shifted to Chonnam National University as an assistant professor in 2019. At present, she has been working on materials science and catalysis for (photo)electrochemical energy conversion.



Kazunari Domen

Kazunari Domen is currently a university professor at The University of Tokyo and special contract professor at Shinshu University, Japan. He received his PhD degree in chemistry from the University of Tokyo in 1982. He joined Chemical Resources Laboratory at Tokyo Institute of Technology in 1982 as an assistant professor and was promoted to an associate professor in 1990 and a professor in 1996. He moved to The University of Tokyo as a

professor in 2004 and was appointed by Shinshu University as a special contract professor in 2017. Since 1980, he has been working on overall water splitting using heterogeneous photocatalysts to produce clean and renewable hydrogen.

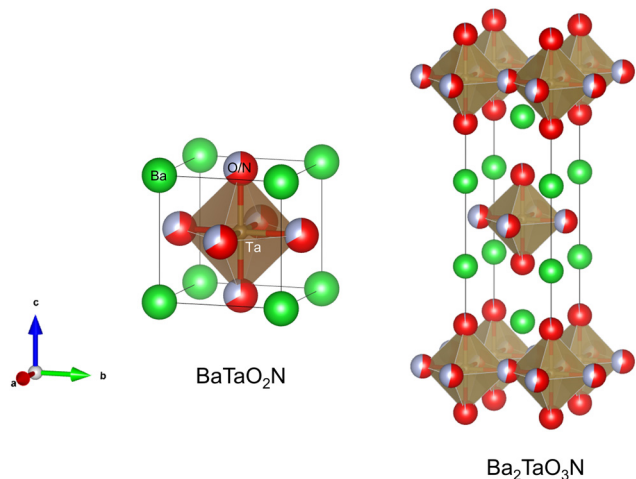


Fig. 1 Crystal structures of perovskite oxynitride  $\text{BaTaO}_2\text{N}$  and Ruddlesden-Popper (RP) phase layered perovskite oxynitride  $\text{Ba}_2\text{TaO}_3\text{N}$ .

perovskite  $\text{AB}(\text{O},\text{N})_3$  whereby the  $\text{B}(\text{O},\text{N})_6$  octahedron is at the center of the cube while the large A atoms occupy the corners. The relationship between the ionic radii ( $r$ ) expressed as  $r_A + r_{(\text{O},\text{N})} = \sqrt{2}(r_B + r_{(\text{O},\text{N})})$  is valid for the ideal cubic perovskite structure. The ratio of left- to right-hand sides of the expression is called the tolerance factor  $t$ , and the ideal cubic perovskites have a  $t$  value of unity. Tilting of the octahedron in the cubic structure originates from the subtle differences between the ionic radii of the cations leading to a  $t$  value less than unity. However, structural distortion producing orthorhombic or tetragonal shapes is commonly found, except for very few combinations including  $\text{BaBO}_2\text{N}$  ( $\text{B} = \text{Ta}$  or  $\text{Nb}$ ). In addition, the perovskite oxynitrides can adopt the  $\text{A}_{1-x-1}\text{A}_{2-x}$  and/or  $\text{B}_{1-y-1}\text{B}_{2-y}$  configurations at the A and/or B sites. In these cases, the stoichiometry of the anions deviates from the ideal coordination configuration if the cations at the A and B sites undergo a change in their oxidation state.

Besides the ideal cubic structure, perovskites can also adopt layered structures in which  $\text{AB}(\text{O},\text{N})_3$  layers are separated by thin layers of intrusive materials (commonly metal oxides), as shown in Fig. 1. Depending on the intruding layers, the perovskite derivatives designated layered perovskites are generally classified as (i) Aurivillius ( $(\text{Bi}_2\text{O}_2)(\text{A}_{n-1}\text{B}_n\text{O}_{3n+1})$ ), (ii) Ruddlesden-Popper (RP) ( $\text{A}_{n+1}\text{B}_n\text{O}_{3n+1}$  or  $\text{A}'\text{A}_{n-1}\text{B}_n\text{O}_{3n+1}$ ), or (iii) Dion-Jacobson ( $\text{A}'\text{A}_{n-1}\text{B}_n\text{O}_{3n+1}$ ) phases ( $n = 1, 2, \text{ or } 3$  represents the number of stacked octahedra separated by a rock salt AO layer). The oxygen in the layered perovskites can be partially exchanged with another anion such as halogen and nitrogen. Sillen-Aurivillius layered perovskite oxyhalides  $\text{A}_4\text{A}'_{n-1}\text{B}_n\text{O}_{3n+5}\text{X}$  ( $\text{A}$  and  $\text{A}' = \text{Sr}, \text{Ba}, \text{Pb}, \text{ or } \text{Bi}$ ;  $\text{B} = \text{Ti}, \text{Nb}, \text{ or } \text{Ta}$ ;  $\text{X} = \text{Cl}$  or  $\text{Br}$ ) were prepared by the substitution of oxygen by halogen.<sup>4,5</sup> Moreover, RP phase oxynitrides  $\text{A}_{n+1}\text{B}_n(\text{O},\text{N})_{3n+1}$  and Dion-Jacobson phase oxynitrides  $\text{A}'\text{A}_{n-1}\text{B}_n(\text{O},\text{N})_{3n+1}$  ( $\text{A} = \text{Ca}, \text{Sr}, \text{Ba}, \text{ or } \text{La}$ ;  $\text{A}' = \text{Li}, \text{Na}, \text{K}, \text{ or } \text{Cs}$ ;  $\text{B} = \text{Ti}, \text{Nb}, \text{ or } \text{Ta}$ ), composed of mixed anions of  $\text{O}^{2-}$  and  $\text{N}^{3-}$ , have been studied as a novel layered perovskite oxynitride family active for various artificial photosynthesis approaches.<sup>6-10</sup>

Perovskite oxides (e.g.,  $\text{SrTiO}_3$ ) and layered perovskite oxides (e.g.,  $\text{Ba}_5\text{Nb}_4\text{O}_{15}$ ) (well-known active catalysts for water splitting to produce  $\text{H}_2$  gas) possess large bandgap energy values ( $E_g$ ) of up to or even above 3.2 eV ( $\lambda < 380$  nm), which are too high to harvest a wide range of the solar spectrum, including visible light.<sup>11-13</sup> Introducing N into the oxide (i.e., nitridation) shifts the valence band maximum (VBM) to a more negative potential because the potential of the N 2p atomic orbitals is lower than that of the O 2p orbitals.<sup>14</sup> Although nitridation leaves the conduction band (CB) potential of the oxide almost unchanged, hybridization of the N 2p and O 2p orbitals during nitridation narrows the  $E_g$  value of the oxide, resulting in a visible-light-responsive perovskite or layered perovskite oxynitride.

The wavelength edges of the visible-light absorption by perovskite oxynitrides vary depending on the combination of cations at the A and B sites, as presented in Fig. 2. For instance,  $\text{SrNbO}_2\text{N}$  can be prepared by the partial exchange of  $3\text{O}^{2-}$  for  $2\text{N}^{3-}$  during the nitridation of layered perovskite  $\text{Sr}_5\text{Nb}_4\text{O}_{15}$ , with the resulting reddish-brown oxynitride  $\text{SrNbO}_2\text{N}$  able to absorb visible light up to a wavelength of approximately 680 nm.<sup>15</sup> In the same manner, in the syntheses of  $\text{SrTaO}_2\text{N}$ ,  $\text{LaTiO}_2\text{N}$ ,  $\text{BaTaO}_2\text{N}$ , and  $\text{BaNbO}_2\text{N}$ , complete nitridation of the corresponding starting oxide resulted in oxynitrides capable of absorbing photons up to ca. 560, 620, 660, and 740 nm, respectively.<sup>16-19</sup> The apparent colors of the oxynitrides became orange, red, dark red, or brown based on their light absorption edge. As discussed previously, the VBM positions of perovskite oxynitrides are composed of hybridized N 2p and O 2p atomic orbitals. The CB minimum (CBM) of the oxynitrides mainly consists of empty Ti 3d, Nb 4d, or Ta 5d orbitals for the

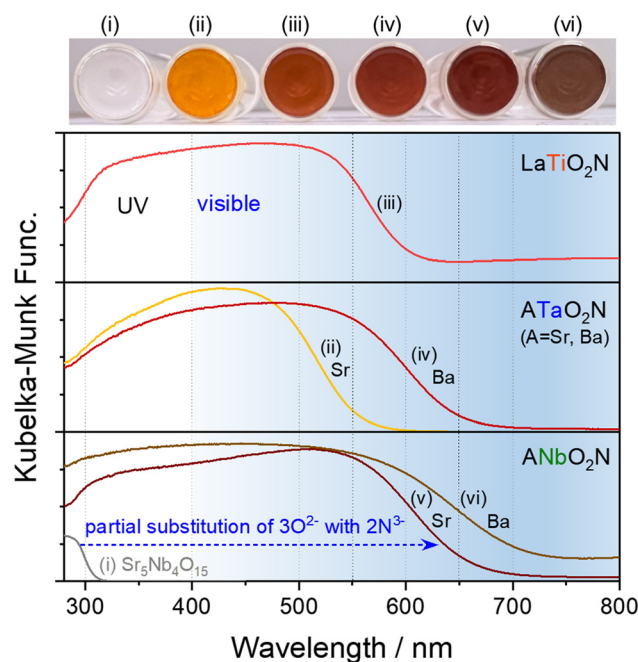


Fig. 2 Photographic images and UV-vis diffuse reflectance spectroscopy (DRS) spectra of perovskite oxynitrides  $\text{AB}(\text{O},\text{N})_3$  ( $\text{A} = \text{Sr}, \text{Ba}, \text{ or } \text{La}$  and  $\text{B} = \text{Ti}, \text{Ta}, \text{ or } \text{Nb}$ ) prepared via nitridation of layered perovskites  $\text{A}_5\text{B}_4\text{O}_{15}$ .

respective B-site cation with  $d^0$  electronic configuration.<sup>20,21</sup> The  $E_g$  value of oxynitrides typically decreases as the effective electronegativity of the B-site cations increases.<sup>21</sup> The effective electronegativity of  $\text{Nb}^{5+}$  is larger than that of  $\text{Ta}^{5+}$ , so Nb-based oxynitrides can absorb longer wavelengths of visible light (Fig. 2). Furthermore, the CBM positions of the oxynitrides are determined by the B–O/N–B bond angles.<sup>21,22</sup> The tilt of the  $\text{B}(\text{O},\text{N})_6$  octahedra in a perovskite structure is larger for a smaller A-site cation, resulting in a narrower CB. The reduced dispersion of the CBs shifts the CBM positions to a more negative potential, thereby causing an increase in  $E_g$ . Thus, the  $E_g$  values of  $\text{BaBO}_2\text{N}$ ,  $\text{SrBO}_2\text{N}$ , and  $\text{CaBO}_2\text{N}$  are sequentially larger according to the size of the A-site cation ( $r_{\text{Ba}} > r_{\text{Sr}} > r_{\text{Ca}}$ ).

In addition to the narrow bandgap, the band positions of the perovskite and layered perovskite oxynitrides straddle the water redox potential (Fig. 3). This indicates that perovskite oxynitrides acting as a single absorber thermodynamically drive overall water splitting to produce  $\text{H}_2$  and  $\text{O}_2$  without the need to supply additional energy for the reaction. The favorable optical properties of the oxynitrides are distinguishable from those of other n-type oxide semiconductors exclusively driving water oxidation, such as visible-light-responsive  $\text{BiVO}_4$  ( $\lambda < 530$  nm) and  $\alpha\text{-Fe}_2\text{O}_3$  ( $\lambda < 600$  nm).<sup>23–25</sup> Moreover, since the CBM potentials of the oxynitrides are more negative than the reduction potential of  $\text{CO}_2$ ,  $\text{HCOOH}$ , carbon monoxide ( $\text{CO}$ ), and methanol ( $\text{CH}_3\text{OH}$ ) can be produced *via* photocatalysis.  $\text{N}_2$  fixation to synthesize  $\text{NH}_3$  gas is theoretically possible *via* photocatalysis with oxynitrides. Finally, since the VBM potentials of the oxynitrides are located below the potential of water oxidation reactions, they can catalyze the oxidation of various anions in seawater (including mineral salts).

Over several decades, perovskite and layered perovskite oxynitrides have been regarded as promising visible-light-responsive semiconductors for efficient artificial photosynthesis to produce value-added eco-friendly and renewable energy resources such as  $\text{H}_2$ ,  $\text{HCOOH}$ ,  $\text{CH}_3\text{OH}$ , and  $\text{NH}_3$ .<sup>2,3,26–28</sup> This is because the oxynitrides are chemically stable in aqueous

electrolytes at various pH values and have ideal optical properties due to a narrow bandgap and a suitable band position, which makes them favorable for sunlight-driven photocatalysis. Therefore, we discuss recent advances in photocatalysis using various perovskite and layered perovskite oxynitrides responsive to a wide wavelength range of the solar spectrum. How the photoactivity of these compounds can be enhanced by their synthesis method for use in photoelectrodes, bulk and surface engineering by doping (or substitution), controlling their morphology, and crystal facet engineering is discussed in detail. We also discuss the challenges associated with using perovskite and layered perovskite oxynitrides for efficient artificial photosynthesis.

## 2. Visible-light-driven photocatalysis

A representative photocatalytic process using perovskite or layered perovskite oxynitrides is water splitting to produce renewable  $\text{H}_2$  energy. The half water oxidation of water splitting typically exhibits very slow kinetics compared with half water reduction so that alternative oxidations using the oxynitrides have been addressed to boost water splitting and then produce  $\text{H}_2$  gas with a higher evolution rate.<sup>29</sup> Recently,  $\text{CO}_2$  reduction using these compounds has also been reported since carbon neutrality is becoming critical globally.<sup>30,31</sup> First, we discuss the various reactions that can be photocatalyzed by perovskite and layered perovskite oxynitrides under sunlight (or only visible-light irradiation), the standard reduction potentials for which are reported in Table 1.

### 2.1. Overall water splitting *via* one-step photoexcitation

The most ideal means of producing  $\text{H}_2$  is overall water splitting using a single semiconductor capable of absorbing visible light. Water redox reactions, *i.e.*, hydrogen evolution reaction (HER) and oxygen evolution reaction (OER), are simultaneously activated at the separate surfaces of a semiconductor particle *via*

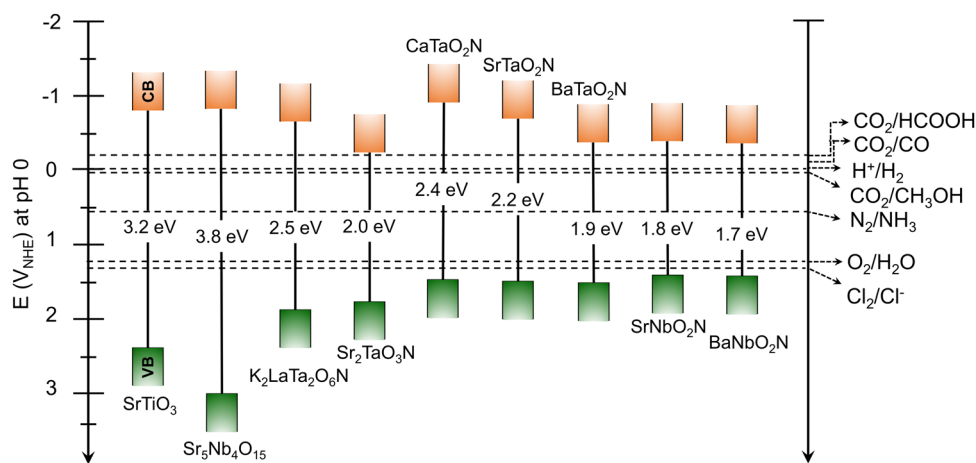
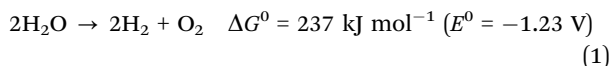


Fig. 3 Bandgap energies (eV) and band edge potentials ( $V_{\text{NHE}}$ ) of representative n-type perovskite and layered perovskite oxynitrides in contact with aqueous electrolytes at pH 0. The electrochemical potentials for  $\text{H}_2$  and  $\text{O}_2$  evolution,  $\text{CO}_2$  reduction,  $\text{Cl}_2$  evolution, and  $\text{N}_2$  fixation are also presented for comparison.

**Table 1** The thermodynamic redox potentials of various reactions that can be photocatalyzed by perovskite and layered perovskite oxynitrides in contact with aqueous electrolytes at pH 0 under sunlight

Half redox reactions	Balanced chemical reactions	Potential ( $V_{\text{NHE}}$ )
CO <sub>2</sub> reduction	$\text{CO}_2 + \text{e}^- \rightleftharpoons \text{CO}_2^-$	-1.90
	$\text{CO}_2 + 2\text{H}^+ + 2\text{e}^- \rightleftharpoons \text{HCOOH}$	-0.20
	$\text{CO}_2 + 2\text{H}^+ + 2\text{e}^- \rightleftharpoons \text{CO} + \text{H}_2\text{O}$	-0.11
	$\text{CO}_2 + 4\text{H}^+ + 4\text{e}^- \rightleftharpoons \text{HCHO} + \text{H}_2\text{O}$	-0.07
	$\text{CO}_2 + 6\text{H}^+ + 6\text{e}^- \rightleftharpoons \text{CH}_3\text{OH} + \text{H}_2\text{O}$	0.03
	$2\text{CO}_2 + 12\text{H}^+ + 12\text{e}^- \rightleftharpoons \text{C}_2\text{H}_5\text{OH} + 3\text{H}_2\text{O}$	0.08
	$\text{CO}_2 + 8\text{H}^+ + 8\text{e}^- \rightleftharpoons \text{CH}_4 + 2\text{H}_2\text{O}$	0.17
Water reduction (HER)	$2\text{H}^+ + 2\text{e}^- \rightleftharpoons \text{H}_2$	0
N <sub>2</sub> reduction	$\text{N}_2 + \text{H}^+ + \text{e}^- \rightleftharpoons \text{N}_2\text{H}$	-3.2
	$\text{N}_2 + 2\text{H}^+ + 2\text{e}^- \rightleftharpoons \text{N}_2\text{H}_2$	-1.1
	$\text{N}_2 + 4\text{H}^+ + 4\text{e}^- \rightleftharpoons \text{N}_2\text{H}_4$	-0.36
	$\text{N}_2 + 8\text{H}^+ + 6\text{e}^- \rightleftharpoons 2\text{NH}_4^+$	0.27
	$\text{N}_2 + 6\text{H}^+ + 6\text{e}^- \rightleftharpoons 2\text{NH}_3$	0.55
Water oxidation (OER)	$\text{O}_2 + 4\text{H}^+ + 4\text{e}^- \rightleftharpoons 2\text{H}_2\text{O}$	1.23
Chloride oxidation (CER)	$\text{Cl}_2 + 2\text{e}^- \rightleftharpoons 2\text{Cl}^-$	1.36
	$\text{ClO}_4^- + 8\text{H}^+ + 8\text{e}^- \rightleftharpoons \text{Cl}^- + 4\text{H}_2\text{O}$	1.39
	$\text{ClO}_3^- + 6\text{H}^+ + 6\text{e}^- \rightleftharpoons \text{Cl}^- + 3\text{H}_2\text{O}$	1.45
	$\text{HClO} + \text{H}^+ + 2\text{e}^- \rightleftharpoons \text{Cl}^- + \text{H}_2\text{O}$	1.48
	$\text{HClO}_2 + 3\text{H}^+ + 4\text{e}^- \rightleftharpoons \text{Cl}^- + 2\text{H}_2\text{O}$	1.57
Hydrogen peroxide production	$\text{H}_2\text{O}_2 + 2\text{H}^+ + 2\text{e}^- \rightleftharpoons 2\text{H}_2\text{O}$	1.78
Sulfate oxidation	$\text{S}_2\text{O}_8^{2-} + 2\text{e}^- \rightleftharpoons 2\text{SO}_4^{2-}$	2.01

one-step photoexcitation to produce H<sub>2</sub> and O<sub>2</sub>, respectively, as follows:



where  $E^0$  is the thermodynamic potential difference for overall water splitting and  $\Delta G^0$  is the Gibbs free energy change. Thus, a semiconductor particle to drive water splitting must have an  $E_g$  greater than 1.23 eV and its band position must span the water redox potentials of 0 and 1.23  $V_{\text{NHE}}$ . As shown in Fig. 3, the thermodynamic characteristics of almost all perovskite and layered perovskite oxynitrides satisfy these requirements, thus making them promising semiconductor candidates for water splitting *via* one-step photoexcitation.

The solar-to-hydrogen (STH) conversion efficiency ( $\eta$ ), a benchmark figure used to estimate the performance of a semiconductor for solar water splitting, is defined by

$$\eta = \frac{\text{output energy as H}_2}{\text{energy of incident solar light}} = \frac{r_{\text{H}_2} (\text{mmol H}_2 \text{ s}^{-1}) \times \Delta G^0 (237\,000 \text{ J mol}^{-1})}{P_{\text{sun}} \times S (\text{cm}^2)} \quad (2)$$

where  $r_{\text{H}_2}$  is the rate of hydrogen evolution,  $P_{\text{sun}}$  is the photon flux of sunlight, and  $S$  is the photoreaction area of a panel or electrode. The STH efficiency greatly depends on the  $E_g$  of the semiconductor, because  $E_g$  determines the photon flux available for water splitting. Fig. 4 presents the relationships between the  $E_g$  values of perovskite oxynitrides and their theoretical maximum STH efficiency, photocurrent, and resulting hydrogen evolution rate per unit area ( $\text{cm}^2$ ). Visible light in the wavelength range of 400–800 nm provides a large proportion of solar energy, and so the STH efficiency is higher in semiconductors with a wider light absorption edge. It is also known that an STH efficiency of 10% and above is required for

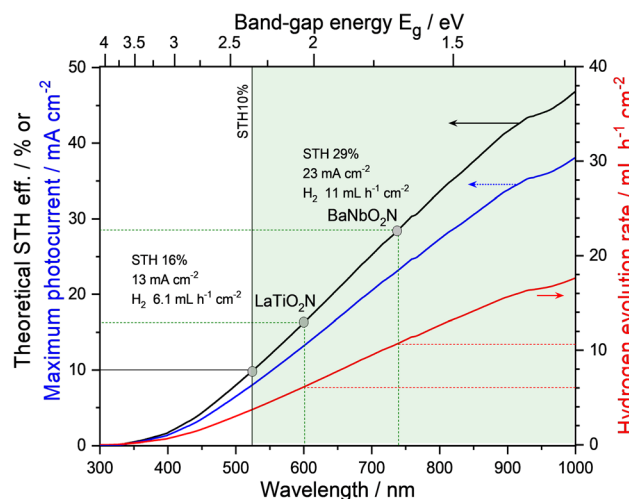


**Fig. 4** A graphical representation of the theoretical maximum solar-to-hydrogen (STH) conversion efficiency, maximum photocurrent density, and hydrogen evolution rate as a function of wavelength. Representative perovskite oxynitrides are positioned along the theoretical STH efficiency curve at their respective absorption edges. The three numerical values beside each perovskite oxynitride indicate the efficiency, photocurrent density, and hydrogen evolution rate.

practical water-splitting applications.<sup>32,33</sup> To satisfy this requirement, the semiconductor as a single absorber should be capable of absorbing visible light up to *ca.* 520 nm without performance loss of the water-splitting device. It is thus noteworthy that besides their suitable band potentials, perovskite and layered perovskite oxynitrides have a small enough  $E_g$  to achieve a high STH efficiency for water splitting. For instance, perovskite LaTiO<sub>2</sub>N ( $E_g = 2.1$  eV) can adsorb visible light up to a wavelength of approximately 600 nm (equivalent to a theoretical STH efficiency of 16%). Moreover, LaTiO<sub>2</sub>N on its own or in a



water-splitting device produces hydrogen gas at  $6.1 \text{ mL h}^{-1} \text{ cm}^{-2}$ , with a maximum photocurrent density of  $13 \text{ mA cm}^{-2}$ . The total photon energy harvested by  $\text{BaNbO}_2\text{N}$  (with an absorption edge of approximately  $740 \text{ nm}$ ) for solar water splitting is much greater than that by  $\text{LaTiO}_2\text{N}$ , resulting in a maximum STH efficiency of 29% corresponding to hydrogen production of  $11 \text{ mL h}^{-1} \text{ cm}^{-2}$ . Thus, it is necessary to develop perovskite and layered perovskite oxynitrides with long light absorption edges of above  $600 \text{ nm}$  to realize commercial water-splitting applications with a high STH value.

Overall water splitting with a quantum efficiency of almost unity using one-step photoexcitation of cuboidal Al-doped  $\text{SrTiO}_3$  ( $\text{SrTiO}_3:\text{Al}$ ) particles with a perovskite crystal structure has been reported.<sup>12</sup> The remarkable water-splitting activity was attributed to the selective depositions of  $\text{Rh}/\text{Cr}_2\text{O}_3$  (for HER) and a  $\text{CoOOH}$  cocatalyst (for OER) at the (100) and (110) crystal facets of  $\text{SrTiO}_3:\text{Al}$ , respectively. HER and OER could be separated and strongly promoted by the anisotropic transport of photogenerated electrons and holes in the single crystal. Overall water splitting on a  $100 \text{ m}^2$  panel comprising modified  $\text{SrTiO}_3:\text{Al}$  particles is an example of a safe mass hydrogen production system with a maximum STH of 0.76%.<sup>34</sup> Although the system design of the panel for scale-up is simple and cost-effective, the low STH efficiency for mass water splitting is still a significant limitation.

Nevertheless, several semiconductors capable of absorbing visible light, such as graphitic- $\text{C}_3\text{N}_4$  ( $E_g = 2.8 \text{ eV}$ ),<sup>37</sup>  $(\text{Ga}_{1-x}\text{Zn}_x)\text{-}(\text{N}_{1-x}\text{O}_x)$  ( $E_g = 2.4 \text{ eV}$ ),<sup>38</sup>  $\text{Ta}_3\text{N}_5$  ( $E_g = 2.1 \text{ eV}$ ),<sup>39</sup> and  $\text{Y}_2\text{Ti}_2\text{O}_5\text{S}_2$

( $E_g = 1.9 \text{ eV}$ ),<sup>40</sup> have been successfully applied to overall water splitting *via* one-step photoexcitation. Moreover, several perovskite oxynitrides have also been utilized. Complex  $\text{LaB}(\text{O},\text{N})_3$  ( $\text{B} = \text{Ta}$  or  $\text{Nb}$ ) solid solutions were successfully employed in the overall water splitting, resulting from the precise tuning of both  $E_g$  and bandgap positions of the oxynitrides *via* the substitution of  $\text{B}^{5+}$  with  $\text{Mg}^{2+}$ .<sup>41,42</sup> These results are discussed in detail in the following section concerning doping (or substitution). Recently, overall water splitting under visible-light irradiation has also been achieved using  $\text{ATaO}_2\text{N}$  ( $\text{A} = \text{Sr}, \text{Ba}$ ) particles with few defects.<sup>35,36</sup> Fig. 5 represents the first demonstration of overall water splitting by particulate  $\text{ATaO}_2\text{N}$  crystals and the corresponding strategies based on the deposition of active cocatalysts. Under Xe lamp irradiation ( $\lambda > 420 \text{ nm}$ ),  $\text{CrO}_x/\text{Ru}/\text{IrO}_2/\text{SrTaO}_2\text{N}$  particles, which are more photoactive than  $\text{BaTaO}_2\text{N}$ , split water to produce  $\text{H}_2$  and  $\text{O}_2$  gases with initial evolution rates of  $9.1$  and  $3.0 \mu\text{mol h}^{-1}$ , respectively.<sup>36</sup> The apparent quantum yield of surface-modified  $\text{SrTaO}_2\text{N}$  at the wavelength of  $420 \pm 30 \text{ nm}$  was 0.34% in the initial stage of water splitting, which became decreasingly saturated to 0.005% during the reaction over 48 h.

Although the  $\text{H}_2$  evolution rate using  $\text{ATaO}_2\text{N}$  particles is very limited compared with that using  $\text{SrTiO}_3:\text{Al}$  particles,<sup>12</sup> it is remarkable that overall water splitting using the perovskite oxynitrides is achieved under visible-light illumination. Interestingly, a general strategy for designing oxynitride particles was employed for overall water splitting *via* one-step photoexcitation. Both perovskite oxynitrides were initially prepared

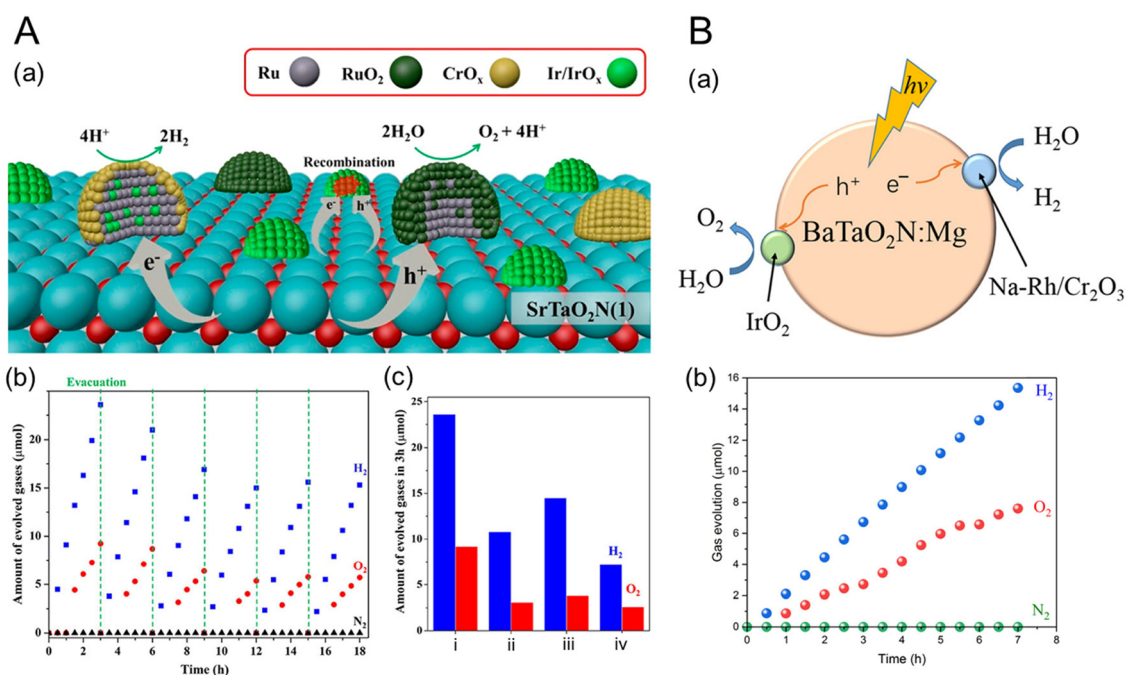


Fig. 5 Overall water splitting by (A) perovskite  $\text{CrO}_x/\text{Ru}/\text{IrO}_2/\text{SrTaO}_2\text{N}$  and (B)  $\text{IrO}_2/\text{Cr}_2\text{O}_3/\text{Na-Rh}/\text{BaTaO}_2\text{N}:\text{Mg}$ . (a) Deposition strategies for the HER and OER cocatalysts and (b) the corresponding gas evolution activities over time under visible-light irradiation ( $\lambda > 420 \text{ nm}$ ) using a 300 W Xe lamp in ultrapure water under an Ar atmosphere with an initial background pressure of 5 or 10 kPa. (c) The amounts of  $\text{H}_2$  and  $\text{O}_2$  gases generated during water splitting for 3 h using  $\text{SrTaO}_2\text{N}$  with various cocatalysts: (i)  $\text{CrO}_x/\text{Ru}/\text{IrO}_2$ , (ii)  $\text{CrO}_x/\text{Ru}$ , (iii)  $\text{CrO}_x/\text{Ru}/\text{IrO}_2(\text{AD})$  (AD: by adsorption of colloidal  $\text{IrO}_2$ ), and (iv)  $\text{IrO}_2/\text{CrO}_x/\text{Ru}$ . Reproduced with permission.<sup>35</sup> Copyright 2022, ACS. Reproduced with permission.<sup>36</sup> Copyright 2023, ACS.

with few defects *via* different synthetic routes. During nitridation, SrCl<sub>2</sub> and NaOH as fluxes, as well as Sr and O as sources, were introduced to obtain SrTaO<sub>2</sub>N with few defects, while doping with Mg<sup>2+</sup> with an Mg/Ta ratio of 0.1 into BaTaO<sub>2</sub>N suppressed the Ta<sub>3</sub>N<sub>5</sub> phase as an impurity. Subsequently, HER and OER cocatalysts were sequentially deposited on the perovskite oxynitride particles to promote the overall water-splitting ability. Ru or Rh covered with CrO<sub>x</sub> or Cr<sub>2</sub>O<sub>3</sub> was employed as the HER catalyst. It is well-known that chromium oxides prevent the reverse reaction (*i.e.*, the oxygen reduction reaction (ORR)) at HER sites.<sup>43,44</sup> RuO<sub>2</sub> or IrO<sub>2</sub> catalysts deposited on the oxynitride surface promoted OER under light irradiation. For overall water splitting, although the bare surfaces of perovskite or layered perovskite oxides with a large bandgap (*e.g.*, SrTiO<sub>3</sub>) can be employed as OER sites for overall water splitting,<sup>11,45</sup> ATaO<sub>2</sub>N particles with a narrow bandgap are still necessary to load the OER cocatalyst. In the solid solution case, a thin coating of amorphous oxyhydroxide on the surface of RhCrO<sub>y</sub>/LaMg<sub>1/3</sub>Ta<sub>2/3</sub>O<sub>2</sub>N suppressed N<sub>2</sub> evolution by self-photooxidation of the oxynitride, thereby improving overall water splitting.<sup>46</sup> Moreover, the deposition of HER and OER cocatalysts on ATaO<sub>2</sub>N particles effectively suppresses the decomposition of the oxynitride and separates the reaction sites. Subsequently, the separation strategy of both types of reaction sites *via* the deposition of cocatalysts is mainly ascribed to the overall water-splitting activity of a single ATaO<sub>2</sub>N particle.

## 2.2. Photoelectrochemical (PEC) water splitting

PEC water splitting using semiconductor electrodes is a potential means of producing H<sub>2</sub> and O<sub>2</sub>. The HER and OER sites are divided into a p-type photocathode and an n-type photoanode, respectively. Based on this, the STH efficiency of a PEC water-splitting cell is typically higher than that of the overall water splitting using a photocatalyst.<sup>47</sup> Various combinations of p- and n-type electrodes have been studied for PEC water splitting without supplying electricity.<sup>48–50</sup> Unbiased PEC water splitting using an inverted and planar lead halide perovskite (LHP) based on the material of a perovskite solar cell (*i.e.*, an NiFe/LHP photoanode and an NiPCoP/LHP photocathode) has recently been reported to generate a high STH conversion efficiency of 10.64% with a photocurrent density of 8.65 mA cm<sup>-2</sup>.<sup>50</sup> A PEC cell using a perovskite BaTaO<sub>2</sub>N photoanode combined with an La<sub>5</sub>Ti<sub>2</sub>Cu<sub>0.9</sub>Ag<sub>0.1</sub>S<sub>5</sub>O<sub>7</sub> photocathode has also shown potential for the unbiased overall water splitting, albeit its activity is very low.<sup>51</sup>

Eqn (2) can be rearranged for the PEC water-splitting system to provide the STH efficiency ( $\eta$ ) as follows:

$$\eta = \frac{|J|(\text{mA cm}^{-2}) \times \eta_{\text{F}} \times 1.23 \text{ V}}{P_{\text{sun}}(\text{mW cm}^{-2})} \quad (3)$$

where  $J$ ,  $\eta_{\text{F}}$ , and  $P_{\text{sun}}$  are the photocurrent density obtained in a two-electrode configuration, faradaic efficiency, and the power density of sunlight (100 mW cm<sup>-2</sup> for AM 1.5G), respectively. According to the definition, a PEC cell must generate high photocurrent density for water splitting without any side

reactions to obtain sufficient STH efficiency. The maximum photocurrent density of the cell is dependent on the  $E_{\text{g}}$  of the semiconductor, and notwithstanding, both photoelectrodes must be responsive to long wavelengths of visible light, as portrayed in Fig. 4. Moreover, the onset potentials for HER and OER at the photocathode and photoanode, respectively, are critical because the STH value of a PEC cell is estimated by using the photocurrent density obtained at the potential where the plotted linear sweep voltammetry (LSV) curves for HER and OER overlap, which is otherwise known as the operation voltage.<sup>3</sup> Thus, a photoanode (or photocathode) capable of both absorbing long wavelengths of visible light and producing a high photocurrent density at a low potential (or high potential) is required for unassisted overall water splitting with high STH efficiency. For efficient water oxidation, the half-cell STH conversion efficiency ( $\eta$ ) of the photoanode (a standard measure) is given by

$$\eta = \frac{|J|(\text{mA cm}^{-2}) \times \eta_{\text{F}} \times (1.23 - V_{\text{app}})(\text{V})}{P_{\text{sun}}(\text{mW cm}^{-2})} \quad (4)$$

where  $J$  is the anodic photocurrent density,  $\eta_{\text{F}}$  is the faradaic efficiency,  $V_{\text{app}}$  is the applied potential, and  $P_{\text{sun}}$  is 100 mW cm<sup>-2</sup> for AM 1.5G. Based on these requirements, n-type perovskite and layered perovskite oxynitrides have been employed as a light absorber for the photoanode in a PEC cell to progress the OER because of their favorable optical property of being responsive to long wavelengths of visible light.<sup>17–19,52</sup>

The B-site cations in perovskite AB(O,N)<sub>3</sub> can easily be reduced to a lower oxidation state (*e.g.*, Nb<sup>5+</sup> to Nb<sup>4+</sup> or Nb<sup>3+</sup>) during high-temperature nitridation under a reducing NH<sub>3</sub> atmosphere owing to their high electronegativity. The reduced B-site cations cause the generation of anion defects and impurity traces that compensate for the charge imbalance, which increases the recombination of photogenerated holes and electrons during water splitting and leads to a decrease in photoactivity. In fact, the photoreaction takes place on the surface of the oxynitride, and surface defects therein negatively influence the PEC water-splitting activity.<sup>18,53</sup> The sunlight-driven PEC activities of LaTiO<sub>2</sub>N, BaNbO<sub>2</sub>N, and BaTaO<sub>2</sub>N photoanodes have been significantly advanced compared to the other perovskite AB(O,N)<sub>3</sub> by controlling the surface defect density.<sup>17–19</sup> Prior to deposition of the OER electrocatalyst, Akiyama *et al.* cleaned the surfaces of synthesized LaTiO<sub>2</sub>N particles by using mild poly(4-styrene sulfonic acid) (PSS) (Fig. 6(A)).<sup>17</sup> This resulted in etching of the defective surface layer of the oxynitride; although longer acid treatment increased the number of fine pores in the surface, it decreased the weight of the oxynitride layer. Afterward, the CoO<sub>x</sub>/LaTiO<sub>2</sub>N photoanode produced a high photocurrent density of 8.9 mA cm<sup>-2</sup> at 1.23 V<sub>RHE</sub> in a 1 M NaOH electrolyte at pH 13.5 under AM 1.5G irradiation, which is the highest reported so far. Moreover, its PEC water-splitting activity was more than two times higher than that of the as-prepared CoO<sub>x</sub>/LaTiO<sub>2</sub>N photoanode. Similarly, eliminating the surface defects in an LaTiO<sub>2</sub>N layer *via* acid treatment with aqua regia doubled the photocatalytic HER and OER activities of the oxynitride particles.<sup>54</sup> Therefore, the effect

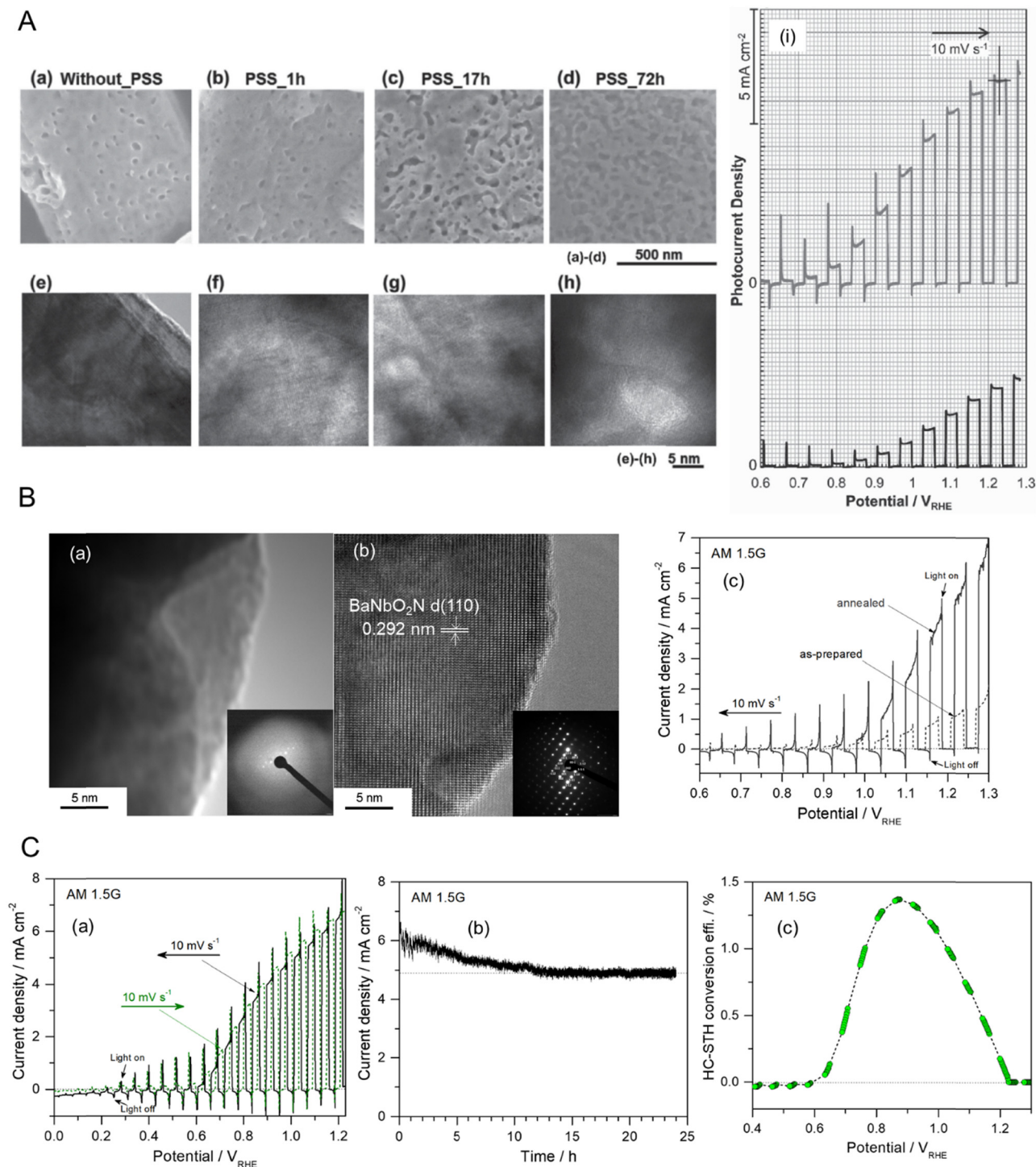


**Fig. 6** PEC water splitting. (A) Scanning electron microscopy (SEM) images (a)–(d) and high-resolution (HR) transmission electron microscopy (TEM) images (e)–(h) of the surface of perovskite  $LaTiO_2N$  treated with poly(4-styrene sulfonic acid) (PSS) for (a), (e) 0, (b), (f) 1, (c), (g) 17, and (d), (h) 72 h. Corresponding linear sweep voltammetry (LSV) curves of  $CoO_x/LaTiO_2N$  photoanodes not treated with PSS for 17 h (upper line) used for PEC water splitting in a 1 M NaOH electrolyte at pH 13.5 under chopped AM 1.5G irradiation. Reproduced with permission.<sup>17</sup> Copyright 2016, Wiley-VCH. (B) HRTEM images of the surface of perovskite  $BaNbO_2N$  as-prepared (a) or annealed under an Ar atmosphere at 873 K for 1 h (b). Corresponding LSV curves of  $Co(OH)_x$ - $FeO_y$ / $BaNbO_2N$  photoanodes used for PEC water splitting in a 0.5 M KBI electrolyte at pH 13 under AM 1.5G irradiation. Reproduced with permission.<sup>18</sup> Copyright 2018, Wiley-VCH. (C) (a) LSV curves in various scan directions of a  $Co(OH)_x$ - $FeO_y$ / $BaTaO_2N$  photoanode annealed under an Ar atmosphere at 1073 K for 1 h after nitridation used for PEC water splitting in a 0.5 M KBI electrolyte at pH 13 under AM 1.5G irradiation. (b) The chronoamperometry curve obtained during long-term water splitting at the applied potential of 1.23  $V_{RHE}$  for 24 h. (c) The half-cell STH (HC-STH) conversion efficiency (%) estimated from the LSV curve presented in (a). Reproduced with permission.<sup>19</sup> Copyright 2019, ACS.



of the acid treatment on photoactivity suggests that an oxynitride surface with a low number of defects is necessary to suppress the recombination of charge carriers and thereby boost water-splitting activity.

In another approach, annealing the surface of perovskite oxynitrides was effective in improving the water-splitting activity of  $\text{Co(OH)}_x\text{-FeO}_y/\text{BaBO}_2\text{N}$  ( $B = \text{Nb, Ta}$ ) photoanodes under sunlight (Fig. 6(B) and (C)).<sup>18,19</sup> The surfaces of the as-prepared oxynitrides were amorphous as a result of mild nitridation of Lewis base Ba-rich  $\text{Ba}_5\text{B}_4\text{O}_{15}$  as the starting oxide. Subsequently, their highly defective surface with a high concentration of oxygen atoms became a single crystal by annealing under an Ar atmosphere at a suitable temperature. For instance, Ar-annealing of  $\text{BaNbO}_2\text{N}$  at 873 K for 1 h resulted in a photocurrent density of  $5.2 \text{ mA cm}^{-2}$  at  $1.23 V_{\text{RHE}}$  for sunlight-driven PEC water splitting in a 0.5 M KBi aqueous electrolyte at pH 13, which is five times higher than that of the as-prepared oxynitride.<sup>18</sup> Although using inert Ar gas has provided the most favorable results, the amorphous surface of oxynitrides can also be crystallized by annealing under other gas atmospheres, such as  $\text{NH}_3$ . The degree of improvement in photoactivity is inversely proportional to the surface defect concentration of the as-prepared oxynitride. Moreover, a highly defective oxynitride surface can become polycrystalline rather than a single crystal *via* Ar-annealing, leading to a small increase in photocurrent. The effect of the annealing temperature on the oxynitride is also dependent on the thermal stability of the oxynitride under an Ar atmosphere.<sup>53</sup> Prolonged annealing at the decomposition temperature of  $\text{BaNbO}_2\text{N}$  ( $> 873 \text{ K}$ ) decreases the photoactivity. For instance, Ar-annealing highly enhanced the surface crystallinity of  $\text{BaTaO}_2\text{N}$ , probably because of its high thermal stability nearly up to 1200 K. Thus, the increased crystallinity of as-prepared bulk  $\text{BaTaO}_2\text{N}$  and its surface *via* Ar-annealing at 1073 K for 1 h induced a high photocurrent density of  $6.5 \text{ mA cm}^{-2}$  at  $1.23 V_{\text{RHE}}$  for water splitting in a 0.5 M KBi aqueous electrolyte at pH 13.<sup>19</sup> The photoactivity of the oxynitride corresponded to a maximum half-cell STH energy conversion efficiency of 1.4% at  $0.88 V_{\text{RHE}}$ , which is still the highest value yet reported using perovskites  $\text{AB(O,N)}_3$ . Moreover, the improved crystallinity both on the surface and in the bulk of  $\text{BaTaO}_2\text{N}$  led to long-term stability during water splitting over 24 h (79% retention of the initial photocurrent). These remarkable results clearly demonstrate that modifying the surface crystallinity of  $\text{AB(O,N)}_3$  *via* annealing or using acid etching to improve the surface texture, both of which lower the defect density, is an excellent way of providing strong separation and fast transfer of photogenerated charges therein, thus leading to highly active and stable PEC water splitting.

### 2.3. Alternative oxidation reactions to the OER

OER driven by four-electron transfer is relatively sluggish compared with HER activated *via* a two-electron pathway, the former creating a bottleneck for water splitting leading to a significant overpotential. The sluggish kinetics of OER typically become much slower in neutral electrolytes regardless of the electrocatalysts and/or semiconductors used, which indirectly causes a low production rate of hydrogen. Alternatively, a high

evolution rate of hydrogen from water at neutral pH can be achieved *via* other oxidation reactions with relatively fast kinetics,<sup>28,55,56</sup> such as the chlorine evolution reaction (CER). In particular, the splitting of seawater with a high concentration (*ca.* 0.55 M) of  $\text{Cl}^-$  involving the CER can be driven under sunlight. In seawater, the thermodynamic potential for the oxidation of  $\text{Cl}^-$  driven *via* two-electron transfer to produce  $\text{Cl}_2$  is  $1.36 V_{\text{NHE}}$  at pH 0 (Table 1). Fig. 7(A) represents a calculated Pourbaix diagram for an artificial chlorine system in a 0.5 M NaCl aqueous electrolyte.<sup>57</sup> The disproportionation of  $\text{Cl}^-$  in water to produce hypochlorous acid ( $\text{HClO}$ ), which is also activated by the two-electron pathway, is possible in the pH range of approximately 3–7.5 while the dissociation of  $\text{HClO}$  producing hypochlorite ( $\text{ClO}^-$ ) occurs at neutral and alkaline pH values because of its  $\text{p}K_a$  of 7.5. Although CER is thermodynamically less favorable than OER ( $E^0 = 1.23 V_{\text{NHE}}$  at pH 0), the oxidation driven *via* the two-electron pathway in the former is kinetically catalyzed faster than in the latter. The CER is selectively more catalyzed than the competing OER even in strong acidic electrolytes due to its independence from the concentration of  $\text{H}^+$ .<sup>58</sup> Moreover, using seawater instead of pure water is cost-effective for artificial  $\text{H}_2$  production systems because the former is very abundant. Based on the advantages of the CER over the OER, PEC seawater splitting using  $\text{WO}_3$  and  $\text{BiVO}_4$  semiconductors at neutral pH has recently been reported.<sup>58–60</sup>

The photoactivity of perovskite oxynitrides for OER is relatively low in neutral electrolytes compared to strong alkaline electrolytes (*e.g.*, at pH 13).<sup>61–63</sup> This is because the band edge and flat band potential energies of  $\text{AB(O,N)}_3$  are dependent on the pH value, and their OER kinetics are very slow under neutral conditions.<sup>14,53</sup> However, the limited activity of  $\text{AB(O,N)}_3$  at a neutral pH makes them unfavorable for commercial water-splitting applications. Recently, the PEC activity of  $\text{SrNbO}_2\text{N}$  for water splitting at a neutral pH was largely enhanced *via* the bottom-up fabrication of the photoanode and the addition of NaCl to an aqueous electrolyte.<sup>29</sup> The feasible mechanism to simultaneously drive the HER and CER using the perovskite oxynitride in artificial seawater is illustrated in Fig. 7(B). The band edge potentials of  $\text{SrNbO}_2\text{N}$  thermodynamically span the standard electrode potential for CER, as well as those for OER and HER, indicating that the holes photogenerated at the surface of the oxynitride are consumed to drive the CER and OER. Fig. 7(C) demonstrates sunlight-driven seawater splitting in a 0.5 M NaCl aqueous electrolyte at pH 6.4 using an  $\text{SrNbO}_2\text{N}$  photoanode prepared *via* bottom-up fabrication including oxidation and flux-assisted nitridation: the oxidation process was necessary for growing the crystalline  $\text{Nb}_2\text{O}_5$  layer on an Nb substrate while the subsequent two-step nitridation process at different temperatures caused the complete conversion of crystalline  $\text{Nb}_2\text{O}_5$  to porous cuboidal  $\text{SrNbO}_2\text{N}$  with high crystallinity and a large surface area. Consequently, the  $\text{Co(OH)}_x/\text{SrNbO}_2\text{N}/\text{Nb}$  photoanode exhibited an mA-level photocurrent in a neutral 0.2 M NaPi aqueous electrolyte, which is a remarkable result for water splitting using a perovskite oxynitride. Moreover, the photoactivity of the oxynitride became three times higher in artificial



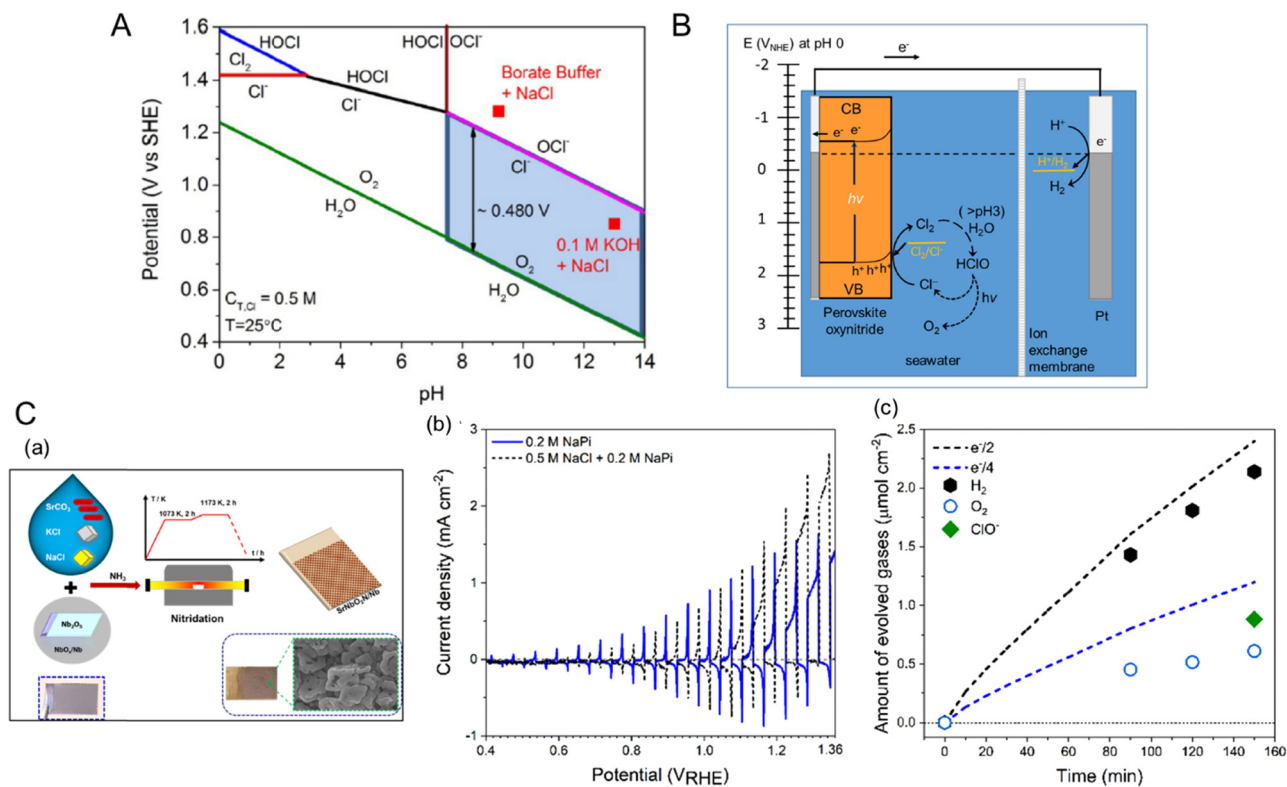
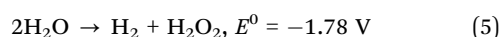


**Fig. 7** Chlorine evolution reaction (CER) in seawater as an alternative oxidation pathway. (A) A computed Pourbaix diagram for an artificial chlorine system in a 0.5 M NaCl aqueous electrolyte without any other mineral salts. Reproduced with permission.<sup>57</sup> Copyright 2016, Wiley-VCH. (B) The feasible mechanism for PEC seawater splitting using a perovskite oxynitride in a 0.5 M NaCl aqueous electrolyte. (C) (a) A schematic of the bottom-up fabrication of an SrNbO<sub>2</sub>N/Nb photoanode involving oxidation and two-step nitridation. (b) LSV curves for the corresponding Co(OH)<sub>x</sub>/SrNbO<sub>2</sub>N/Nb photoanode during seawater splitting in a 0.2 M NaPi buffer with and without 0.5 M NaCl electrolyte (at pH 6.4 and 6.7, respectively) under AM 1.5G irradiation. (c) Time courses of O<sub>2</sub>, ClO<sup>-</sup>, and H<sub>2</sub> generation during seawater splitting using the same photoanode and a Pt wire at an applied potential of 1.23 V<sub>RHE</sub> in a 0.5 M NaCl electrolyte buffered with 0.2 M NaPi under AM 1.5G simulated sunlight for 150 min. The dashed lines indicate the amounts of H<sub>2</sub>, ClO<sup>-</sup> (e<sup>-</sup>/2), and O<sub>2</sub> (e<sup>-</sup>/4) estimated for a faradaic efficiency of unity. Reproduced with permission.<sup>29</sup> Copyright 2023, ACS.

seawater including 0.5 M NaCl providing the activation of the CER as well as the OER. Quantitative analysis proved that seawater splitting by SrNbO<sub>2</sub>N resulted in the generation of HClO, ClO<sup>-</sup>, and O<sub>2</sub> in the oxidation compartment and H<sub>2</sub> evolution in the reduction compartment, corresponding to a faradaic efficiency of almost 90%. These results clearly indicate that the CER is more preferentially driven over the OER during seawater splitting at neutral pH. It also indicates that the CER can be an alternative oxidation reaction to the OER that improves the H<sub>2</sub> production activity of perovskite oxynitrides in strong alkaline to neutral environments.

Hydrogen peroxide (H<sub>2</sub>O<sub>2</sub>) production from water oxidation is regarded as an alternative oxidation reaction to the OER,<sup>28,64</sup> and H<sub>2</sub>O<sub>2</sub> is also generated *via* the ORR using semiconductor photocathodes.<sup>65,66</sup> In this review, we only discuss H<sub>2</sub>O<sub>2</sub> production from water oxidation in terms of improving H<sub>2</sub> production. As reported in Table 1, although H<sub>2</sub>O<sub>2</sub> production is driven *via* a two-electron pathway similar to the CER leading to kinetically fast activation, its thermodynamic potential of 1.78 V<sub>NHE</sub> is significantly unfavorable compared with the competing OER. The overall reaction for H<sub>2</sub>O<sub>2</sub> production and water reduction *via* one-step photoexcitation is as follows:



Despite the thermodynamic disadvantage, the production of H<sub>2</sub>O<sub>2</sub> based on the photocatalytic oxidation of water has recently been attempted because H<sub>2</sub>O<sub>2</sub> is a much higher value-added product than O<sub>2</sub>.<sup>67–69</sup> Moreover, attempts at suppressing the competitive OER and selectively improving the valuable H<sub>2</sub>O<sub>2</sub> production have been successful. In particular, it has been reported that the HCO<sub>3</sub><sup>-</sup> electrolyte in the pH range of 7–8 promotes the PEC activity of a BiVO<sub>4</sub>/WO<sub>3</sub> photoanode for H<sub>2</sub>O<sub>2</sub> production.<sup>70</sup> However, the very low faradaic efficiency for the PEC H<sub>2</sub>O<sub>2</sub> production (approximately 54%) was improved up to 79% by introducing an Al<sub>2</sub>O<sub>3</sub> overlayer on the photoanode.<sup>67</sup> In the reaction mechanism, the weakly basic HCO<sub>3</sub><sup>-</sup> as a hole acceptor is adsorbed at the weakly acidic Al<sub>2</sub>O<sub>3</sub> surface and oxidized to unstable HCO<sub>4</sub><sup>-</sup>, which then reacts with H<sub>2</sub>O to produce H<sub>2</sub>O<sub>2</sub>. Furthermore, a faradaic efficiency of more than 90% for H<sub>2</sub>O<sub>2</sub> production using the Gd-doped BiVO<sub>4</sub> photoanode in the potential range of 1.8–2.5 V<sub>RHE</sub> has been reported.<sup>69</sup> The authors theorized that the Gd doping of BiVO<sub>4</sub> shifted the binding energy of OH<sup>-</sup> on the active sites of Bi–Bi to a more optimal energy level, thereby boosting H<sub>2</sub>O<sub>2</sub> production. Although the catalytic mechanism for H<sub>2</sub>O<sub>2</sub> production is still

uncertain,<sup>64</sup> it is remarkable that the selectivity and faradaic efficiency of the H<sub>2</sub>O<sub>2</sub> production can be highly improved despite its unfavorable thermodynamic characteristics compared with the OER.

Although semiconductors with a wide bandgap (*e.g.*, TiO<sub>2</sub>, WO<sub>3</sub>, and BiVO<sub>4</sub>) have been employed as photocatalysts or photoelectrodes for H<sub>2</sub>O<sub>2</sub> production,<sup>28,64,65</sup> photocatalytic oxidation to produce valuable H<sub>2</sub>O<sub>2</sub> using perovskite or layered perovskite oxynitrides has not yet been reported. Based on the electromotive force of H<sub>2</sub>O<sub>2</sub> production (1.78 V) being higher than that of water splitting, the band structures of perovskite oxynitrides with a negative VBM potential could make them unsuitable. However, the band structures of layered perovskite oxynitrides with relatively large  $E_g$  values possibly make them suitable for H<sub>2</sub>O<sub>2</sub> production (Fig. 3). Moreover, the bandgap engineering of perovskite oxynitrides *via* substitution with alien elements could make them capable of thermodynamically driving H<sub>2</sub>O<sub>2</sub> production.<sup>41,46</sup> Therefore, in addition to CER, H<sub>2</sub>O<sub>2</sub> production using perovskite or layered perovskite oxynitrides may be an alternative oxidation reaction to OER that efficiently produces not only valuable H<sub>2</sub>O<sub>2</sub> but also H<sub>2</sub>.

#### 2.4. CO<sub>2</sub> reduction

The photocatalytic reduction of CO<sub>2</sub> using a semiconductor is driven *via* a multiple-electron transfer process that generates many different products, such as formic acid (HCOOH), carbon monoxide (CO), methanol (CH<sub>3</sub>OH), methane (CH<sub>4</sub>), and so on, depending on the number of transferred electrons and the subsequent reaction pathway (Table 1). The catalytic mechanism is complex and has been unclear until very recently. Indeed, much research effort toward understanding it and increasing the selectivity for its high-value reaction products has been made because of the current global drive toward carbon neutrality.<sup>71–73</sup> Photocatalytic and PEC systems employing perovskite or layered perovskite oxynitrides for CO<sub>2</sub> reduction under visible-light irradiation have also been reported.<sup>30,74</sup>

The band edge potentials of perovskite and layered perovskite oxynitrides straddling the various CO<sub>2</sub> reduction potentials

in Fig. 3 suggest their suitability as a semiconductor for sunlight-driven CO<sub>2</sub> reduction. In fact, the overall reaction including the CO<sub>2</sub> reduction and OER in (sea)water containing dissolved CO<sub>2</sub> catalyzed by oxynitrides is thermodynamically feasible *via* one-step photoexcitation. However, this has still not been realized because of the small driving force of oxynitrides with a narrow bandgap for CO<sub>2</sub> reduction and sluggish OER kinetics driven *via* the simultaneous transfer of four electrons. Alternatively, a hybrid PEC cell constructed using a CuGaO<sub>2</sub>/PRu-Re photocathode and a CoO<sub>x</sub>/TaON photoanode exhibited visible-light-driven CO<sub>2</sub> reduction to produce CO and oxidation *via* the OER to release O<sub>2</sub> in an aqueous electrolyte with no external bias,<sup>75</sup> albeit the efficiency of the system was very poor.

In the study by Yoshitomi *et al.*, although triethanolamine (TEOA) in an organic solvent instead of water was used as the hole acceptor, a hybrid perovskite CaTaO<sub>2</sub>N coupled with a binuclear Ru(II) complex (RuRu') catalyst activated CO<sub>2</sub> reduction under visible-light illumination to produce HCOOH with high selectivity.<sup>76</sup> Fig. 8(A) illustrates the expected Z-scheme CO<sub>2</sub> reduction mechanism of the hybrid catalyst under visible light. The binuclear RuRu' complex is composed of a redox photosensitizer unit (Ru(PS)) and a catalytic unit (Ru(Cat)). Both CaTaO<sub>2</sub>N and RuRu' are capable of absorbing visible light up to a wavelength of 500 nm. The authors proposed that the transfer of photoexcited electrons from the CBM potential of CaTaO<sub>2</sub>N to Ru(PS) and then to Ru(Cat) provides the Z-scheme for CO<sub>2</sub> reduction. The effect of each component in the hybrid catalyst on the CO<sub>2</sub> reduction activity is summarized in Table 2. The combination of CaTaO<sub>2</sub>N with RuRu' exclusively enabled the detection of formate resulting from the dissociation of HCOOH with a high selectivity of greater than 99%. The oxynitride with only Ru(Cat) adsorbed thereon produced less formate and accompanying byproduct H<sub>2</sub>, while its combination with Ru(PS) did not produce either product. These results indicate that both CaTaO<sub>2</sub>N and the binuclear RuRu' complex were necessary to realize HCOOH production. Moreover, the deposition of Ag particles on the CaTaO<sub>2</sub>N surface resulted in three times higher CO<sub>2</sub> reduction

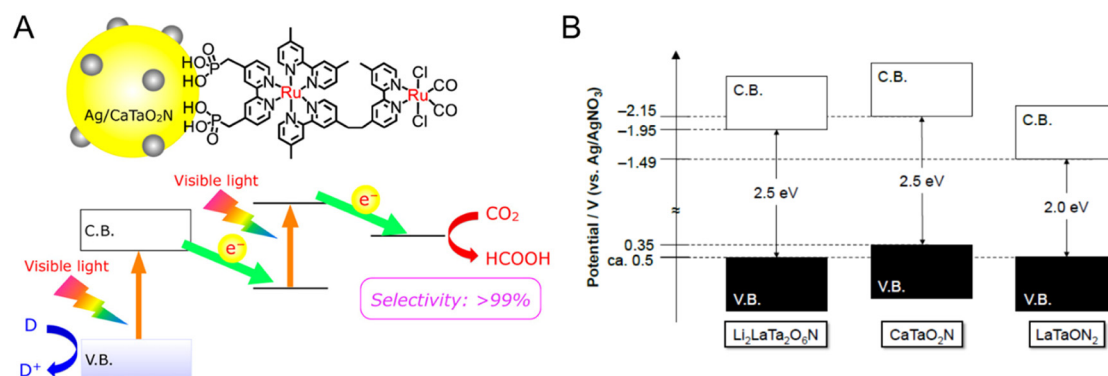


**Fig. 8** CO<sub>2</sub> reduction. (A) The catalytic mechanism for visible-light-driven Z-scheme CO<sub>2</sub> reduction using a hybrid catalyst consisting of perovskite and layered perovskite oxynitrides and a binuclear Ru complex (RuRu'). Reproduced with permission.<sup>76</sup> Copyright 2015, ACS. (B) Band structure diagrams of layered perovskite Li<sub>2</sub>LaTa<sub>2</sub>O<sub>6</sub>N and perovskites CaTaO<sub>2</sub>N and LaTaON<sub>2</sub> estimated in an anhydrous acetonitrile (MeCN) electrolyte containing 0.1 M tetraethylammonium tetrafluoroborate (Et<sub>4</sub>NBF<sub>4</sub>) at pH 7. Reproduced with permission.<sup>26</sup> Copyright 2018, Wiley-VCH.

**Table 2** The photocatalytic CO<sub>2</sub> reduction activity of various hybrid catalysts consisting of perovskite or layered perovskite oxynitrides and a binuclear Ru complex (RuRu'). Reproduced with permission.<sup>26</sup> Copyright 2018, Wiley-VCH. Reproduced with permission.<sup>76</sup> Copyright 2015, ACS

Parameter	Photocatalyst <sup>a</sup>	Product amount (nmol)		
		Formate	H <sub>2</sub>	Selectivity for formate (%)
Reaction medium	CaTaO <sub>2</sub> N	ND	ND	—
	Ag/CaTaO <sub>2</sub> N	ND	ND	—
	RuRu'	ND	ND	—
	RuRu'/CaTaO <sub>2</sub> N	93	ND	—
Ag	RuRu'/Ag/CaTaO <sub>2</sub> N	320	ND	> 99
	Ru(Cat)/Ag/CaTaO <sub>2</sub> N	114	2.6	—
RuRu'	Ru(PS)/Ag/CaTaO <sub>2</sub> N	ND	3.8	—
	Ru(Cat)/Ag/CaTaO <sub>2</sub> N	114	2.6	—
Semiconductor <sup>b</sup>	Li <sub>2</sub> LaTa <sub>2</sub> O <sub>6</sub> N	ND	ND	—
	RuRu'/LaTaON <sub>2</sub>	ND	ND	—
	RuRu'/Li <sub>2</sub> LaTa <sub>2</sub> O <sub>6</sub> N	660	16	97
	RuRu'/Ag/Li <sub>2</sub> LaTa <sub>2</sub> O <sub>6</sub> N	1440	16	99

<sup>a</sup> Reaction conditions: CO<sub>2</sub> reduction for 15 h using 4.0 mg of photocatalyst in a CO<sub>2</sub>-purged *N,N*-dimethylacetamide (DMA)/triethanolamine (TEOA) (4:1 v/v) electrolyte of 4 mL under a 400 W high-pressure Hg lamp with a filter comprising sodium nitrite (NaNO<sub>2</sub>) solution. In each case, the adsorbed amount of RuRu' and the loading amount of Ag on the semiconductor were 2.5 μmol g<sup>-1</sup> and 1.0 wt%, respectively. <sup>b</sup> The semiconductor upon which 3 μmol g<sup>-1</sup> of RuRu' was adsorbed was immersed in mixed anhydrous acetonitrile (MeCN)/TEOA (4:1 v/v). RuRu' is composed of a redox photosensitized unit (Ru(PS)) and a catalytic unit (Ru(Cat)). ND, not detected.

activity. The metallic Ag particles did not act as a cocatalyst but instead as an intermediate promoter by accumulating photo-generated electrons and then mediating charge transfer from CaTaO<sub>2</sub>N to RuRu'. This high activation and selectivity for visible-light-driven CO<sub>2</sub> reduction can be attributed to fast electron transfer caused by the suitable arrangement of the energy levels of CaTaO<sub>2</sub>N and RuRu' and by the deposition of Ag particles.

It has been reported that visible-light-driven CO<sub>2</sub> reduction can be highly activated by introducing a 2D-layered perovskite Li<sub>2</sub>LaTa<sub>2</sub>O<sub>6</sub>N instead of CaTaO<sub>2</sub>N.<sup>26</sup> Although the *E<sub>g</sub>* value of layered perovskite Li<sub>2</sub>LaTa<sub>2</sub>O<sub>6</sub>N is the same as that of CaTaO<sub>2</sub>N, its band structure is slightly shifted to a more positive potential from that of the perovskite oxynitride due to its different A-site cations and lower concentration of nitrogen (Fig. 8(B)). According to the CO<sub>2</sub> reduction activity reported in Table 2, the CBM potential of Li<sub>2</sub>LaTa<sub>2</sub>O<sub>6</sub>N, even though reduced, is sufficient to transfer photogenerated electrons to RuRu'. The tendency for the photoactivity of Li<sub>2</sub>LaTa<sub>2</sub>O<sub>6</sub>N is identical to that of CaTaO<sub>2</sub>N, *i.e.*, the combination with RuRu' and the deposition of Ag nanoparticles thereon are essential for driving the photo-reaction with high selectivity. Interestingly, the CO<sub>2</sub> reduction activity using Li<sub>2</sub>LaTa<sub>2</sub>O<sub>6</sub>N was almost five times higher than that using CaTaO<sub>2</sub>N. The largely enhanced photoactivity was mainly ascribed to the high crystallinity of Li<sub>2</sub>LaTa<sub>2</sub>O<sub>6</sub>N with a lower density of defect traps and higher density of reactive electrons, as analyzed by using transient absorption spectroscopy. However, the effect of the 2D structure of Li<sub>2</sub>LaTa<sub>2</sub>O<sub>6</sub>N on the photoactivity has not yet been elucidated.<sup>9,77</sup>

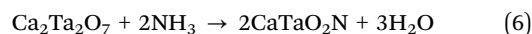
Perovskite oxynitrides employed as a single photocatalyst rather than in a hybrid catalyst with organic compounds for visible-light-driven CO<sub>2</sub> reduction have recently been reported.<sup>78–80</sup> The deposition of a core-shell Ni-Ag bicomponent cocatalyst on CaTaO<sub>2</sub>N increased interfacial electron transfer and thus enhanced the CO<sub>2</sub> reduction activity, showing a synergistic effect of the bicomponent catalyst.<sup>78</sup> Moreover, heterojunction structures composed of a metal oxide (*e.g.*, CeO<sub>2</sub>) and LaTiO<sub>2</sub>N have been

shown to improve CO<sub>2</sub> reduction, which is a well-known strategy for effectively suppressing the recombination of photo-generated charges and thereby boosting the photoreaction.<sup>79,80</sup> This approach for CO<sub>2</sub> reduction mainly results in CO production accompanied by CH<sub>4</sub> as a secondary product, thereby indicating relatively low selectivity for them. Therefore, there is still room for improvement in sunlight-driven CO<sub>2</sub> reduction activity and product selectivity using perovskite and layered perovskite oxynitrides. Nevertheless, successful CO<sub>2</sub> reduction using the oxynitrides also demonstrates the suitability of their band structures for various artificial photosynthetic processes and H<sub>2</sub> production *via* water splitting.

### 3. Synthesis of perovskite and layered perovskite oxynitrides

#### 3.1. Powder

Perovskite and layered perovskite oxynitrides are typically prepared *via* high-temperature nitridation of the starting oxides with a stoichiometric A/B ratio identical to that of the resulting oxynitride under an NH<sub>3</sub> atmosphere (*e.g.*, Ca<sub>2</sub>Ta<sub>2</sub>O<sub>7</sub> for CaTaO<sub>2</sub>N, Sr<sub>2</sub>Nb<sub>2</sub>O<sub>7</sub> for SrNbO<sub>2</sub>N, or amorphous Sr<sub>2</sub>TaO<sub>x</sub> for Sr<sub>2</sub>TaO<sub>3</sub>N).<sup>81–83</sup> During nitridation, NH<sub>3</sub> thermally decomposes into H<sub>2</sub> and N<sub>2</sub>, and N<sup>3-</sup> from N<sub>2</sub> exchanges with O<sup>2-</sup> in the starting oxide under the reducing atmosphere exemplified in the following equation for CaTaO<sub>2</sub>N synthesis:



Otherwise, the oxynitrides are synthesized *via* calcination of the starting nitride precursor under an inert N<sub>2</sub>/Ar atmosphere. For instance, BaTaO<sub>2</sub>N has been prepared using TaN as the Ta precursor based on the following reaction:<sup>84</sup>



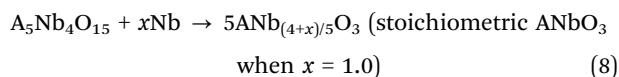
The ammonium chloride (NH<sub>4</sub>Cl) powder instead of toxic NH<sub>3</sub> gas has also been used as the nitrogen source for



nitridation because it thermally decomposes into  $\text{NH}_3$  and  $\text{HCl}$  at a temperature higher than 610 K.<sup>85</sup>

**3.1.1. Polymerized-complex method.** Commonly prepared *via* a solid-state reaction (SSR), the crystalline starting oxide with a cation ratio stoichiometric to the corresponding oxynitride is completely converted to the latter according to eqn (6). For multi-metal oxynitrides such as  $\text{LaMg}_x\text{Ta}_{1-x}\text{O}_{1+3x}\text{N}_{2-3x}$  and  $\text{K}_2\text{LaTa}_2\text{O}_6\text{N}$ , it is difficult to prepare the single-crystalline starting oxide *via* an SSR without traces of impurities. Fortunately, a polymerized-complex method is a facile means of preparing homogeneous starting mixed oxides at the atomic level for nitridation to oxynitrides.<sup>41,86,87</sup> In short, citric acid and/or ethylene glycol are blended in methanol in which the metal precursors for the A- and B-site cations are dissolved, followed by heating to catalyze polymerization. The resulting transparent or yellow resin (proof of polymerization) is carbonized at a low temperature ( $\leq 773$  K) to remove the organic chain in the resin. Subsequently, the carbonized powder is calcined at a higher temperature ( $\geq 1073$  K) to finally yield a homogeneous white oxide; if it has a crystalline structure, the particle size can be controlled by varying the calcination temperature.<sup>88</sup> The homogeneous starting oxides are easily transformed *via* nitridation to the corresponding oxynitride with a single perovskite or layered perovskite structure that is responsive to visible light. Moreover, the resulting oxynitride is capable of water splitting and other artificial photosynthesis processes.<sup>26,41,42,83,89</sup> The polymerized-complex method is effective at preparing oxynitrides with small particles and high crystallinity that provide many catalytic sites to drive photoreactions.<sup>41,42</sup>

**3.1.2. Conversion of A-site cation-rich starting oxides.** The high crystallinity of a semiconductor is typically a critical factor for suppressing the recombination of photogenerated charges and promoting their separation and fast transfer. Many attempts to prepare perovskite and layered perovskite oxynitrides with high crystallinity and without impurity phases have been reported.<sup>62,91–93</sup> It is typical that the stoichiometric oxides prepared *via* SSR form crystalline oxynitrides. If the stoichiometric oxide has a crystal structure different from the corresponding oxynitride, then the conversion of the crystal oxide phase to the perovskite or layered perovskite will definitely go ahead during nitridation. This can require a long nitridation period, which sometimes results in a low-crystalline perovskite oxynitride with a high density of defects.<sup>94,95</sup> Moreover, exceptional oxynitrides such as  $\text{BaBO}_2\text{N}$  (B = Ta, Nb) have no corresponding starting stoichiometric crystalline oxide, so an amorphous mixture of oxides of all the elements within the oxynitride must be used instead.<sup>91,96</sup> Particulate  $\text{ANbO}_2\text{N}$  (A = Sr, Ba) can be prepared from the nitridation of stoichiometric perovskite  $\text{ANbO}_3$  ( $\text{Nb}^{4+}$ ), as shown in Fig. 9(A).<sup>90</sup> Cubic perovskite  $\text{SrNbO}_3$  is a red metallic photocatalyst for photocatalytic  $\text{H}_2$  and  $\text{O}_2$  evolution under visible light ( $\lambda > 420$  nm).<sup>97</sup> Single-phase  $\text{ANbO}_3$  can be synthesized in sealed evacuated fused quartz ampoules through the following reaction:



The SEM images in Fig. 9(B) and the XRD patterns in Fig. 9(C)-(a) show the transformation of smooth perovskite  $\text{BaNbO}_3$  to randomly porous  $\text{BaNbO}_2\text{N}$  *via* nitridation at 1173 K for 20 h. The perovskite  $\text{BaNbO}_3$  was monotonically converted to perovskite oxynitride  $\text{BaNbO}_2\text{N}$  without involving any structural transition, leading to the exchange of oxygen with nitrogen. Thus, the use of  $\text{ANbO}_3$  as the starting precursor was effective in the preparation of surface- and bulk-crystalline  $\text{ANbO}_2\text{N}$ . Nevertheless, the high water-splitting activity of  $\text{ANbO}_2\text{N}$  was not achieved from stoichiometric  $\text{ANbO}_3$  (as  $x = 1.0$ ). The high bulk crystallinity of  $\text{ANbO}_2\text{N}$  was accompanied by an impurity phase of  $\text{NbO}_x\text{N}_y$  and a surface concentration ratio of A/Nb lower than unity, resulting in an oxynitride with rather low photoactivity. An A-site-rich oxide (as  $x < 1.0$ ) was necessary to obtain stoichiometric oxynitrides without the impurity phase because of the volatility of the A-site cation in the presence of alkali and alkali-earth metal groups during high-temperature nitridation. In response, the use of A-site-rich precursors has been applied in various syntheses of perovskite and layered perovskite oxynitrides.<sup>62,94–96</sup> Layered perovskite  $\text{A}_5\text{B}_4\text{O}_{15}$  (A = Sr, Ba; B = Ta, Nb) has been employed in the synthesis of photoactive  $\text{ABO}_2\text{N}$ , as presented in Fig. 9(A).<sup>15,18,19</sup> The starting oxides have a crystal structure similar to that of  $\text{ABO}_2\text{N}$ , with the A-rich concentration being replenished during high-temperature nitridation to compensate for the volatility of the A-site cations. The layered perovskite was converted to perovskite oxynitride  $\text{ABO}_2\text{N}$  *via* the following reaction:



The smooth-layered perovskites were completely changed to their porous  $\text{ABO}_2\text{N}$  counterpart *via* a process analogous to the conversion of perovskite  $\text{ANbO}_3$ . However, they are distinguishable in that the pores are orderly located in a layered structure, probably resulting from the decomposition of an AO layer in  $\text{A}_5\text{B}_4\text{O}_{15}$  and the exchange of three  $\text{O}^{2-}$  ions in the equatorial planes of octahedral  $\text{BO}_6$  with two  $\text{N}^{3-}$  (Fig. 9(B)).<sup>98</sup> As shown in Fig. 9(C)-(b), (c), the transformation of  $\text{A}_5\text{Nb}_4\text{O}_{15}$  to  $\text{ANbO}_2\text{N}$  was completed with no AO impurity traces after 15 h of nitridation.<sup>15</sup> The excess of A species, undoubtedly in the form of the amorphous phase and/or nanoparticles, was easily removed with distilled water in the washing step of  $\text{ANbO}_2\text{N}$  due to the A species being a Lewis base. The Lewis base A-rich species positively suppressed the reduction of the B-site cation, leading to  $\text{ABO}_2\text{N}$  with fewer defects and an adjusted stoichiometric A/B ratio in the oxynitride. However, it caused an amorphous surface to form on  $\text{ABO}_2\text{N}$ , which became crystalline *via* subsequent Ar-annealing treatment at a suitable temperature depending on the thermal property of  $\text{ABO}_2\text{N}$  that enhanced water-splitting photoactivity. In another conversion, employing a  $(\text{Na}_{1/4}\text{Ba}_{3/4})(\text{Zn}_{1/4}\text{Ta}_{3/4})\text{O}_3$  solid solution with a perovskite structure to synthesize active  $\text{BaTaO}_2\text{N}$  maximized the evaporation of volatile Na and Zn elements during nitridation.<sup>99</sup>

**3.1.3. Flux-assisted calcination/nitridation.** Flux-assisted nitridation using additive molten salts, as well as the adoption of suitable starting precursors, is an effective way of preparing

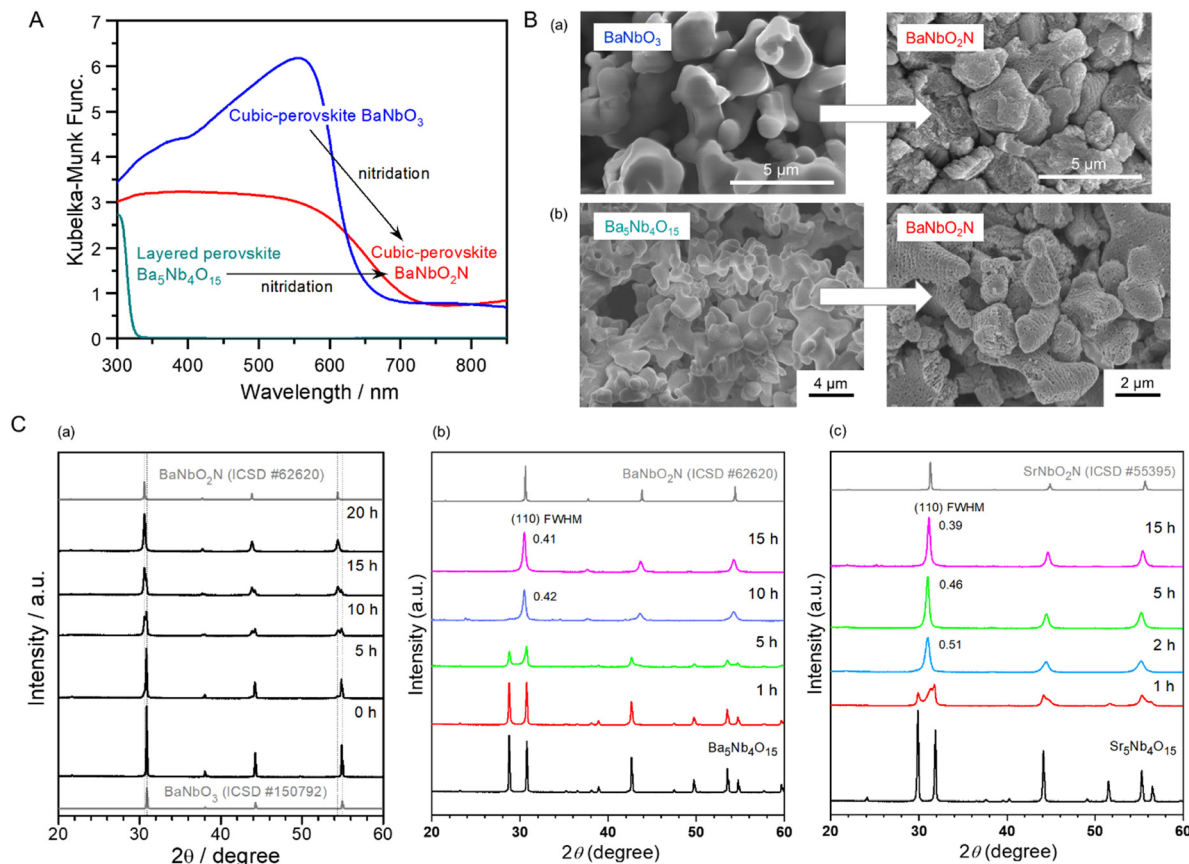
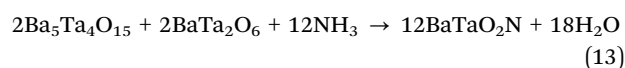
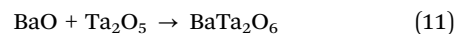


**Fig. 9** Conversion of perovskite  $\text{BaNbO}_3$  and layered perovskite  $\text{Ba}_5\text{Nb}_4\text{O}_{15}$  to  $\text{BaNbO}_2\text{N}$  via nitridation. (A) UV-vis (DRS) spectra of starting  $\text{BaNbO}_3$  and  $\text{Ba}_5\text{Nb}_4\text{O}_{15}$  oxides for the synthesis of visible-light-responsive  $\text{BaNbO}_2\text{N}$ . (B) SEM images of the different starting oxides and the corresponding oxynitrides after nitridation. (C) X-ray diffraction (XRD) patterns for perovskite  $\text{ANbO}_2\text{N}$  ( $A =$  (a), (b) Ba, (c) Sr) and intermediate derivatives obtained via the nitridation of (a)  $\text{BaNbO}_3$  and (b), (c)  $\text{A}_5\text{Nb}_4\text{O}_{15}$  at 1123 and 1173 K, respectively. FWHM, full-width at half-maximum. Reproduced with permission.<sup>15</sup> Copyright 2022, Elsevier. Reproduced with permission.<sup>90</sup> Copyright 2016, ACS.

highly crystalline perovskite and layered perovskite oxynitrides. The molten fluxes produced during high-temperature nitridation are employed as a solvent for crystallization of the oxynitrides. It is well-known that the solubility of the solute (*i.e.*, the cation precursors of oxynitrides), which determines the crystallinity and surface morphology of the resulting product (*i.e.*, the oxynitride), is influenced by the solute-to-flux molar ratio, operating temperature, and nitridation duration.<sup>100,101</sup> Oxynitrides are commonly synthesized *via* the flux-assisted nitridation of the corresponding precursors in a single step or the crystalline oxide precursors prepared *via* flux-assisted calcination in two steps. Single-crystalline  $\text{LaTaON}_2$  prepared *via* a one-step flux method using KCl exhibited higher photocatalytic and PEC activity than those prepared *via* polymerized-complex and SSR methods because of the reduced defect density and enhanced crystallinity of the oxynitride.<sup>102</sup> Furthermore, perovskite  $\text{SrNbO}_2\text{N}$  prepared *via* one- or two-step flux-assisted nitridation became highly crystalline and the resulting oxynitride prepared from the corresponding oxide through NaI-assisted calcination provided an excellent photocurrent density of  $1.5 \text{ mA cm}^{-2}$  at  $1.23 V_{\text{RHE}}$  under AM 1.5G simulated sunlight.<sup>93</sup> Crystalline  $\text{BaNbO}_2\text{N}$  particles prepared *via* the

nitridation of  $\text{Ba}_5\text{Nb}_4\text{O}_{15}$  and subsequent NaCl-assisted calcination provided significantly high photocatalytic OER activity under visible-light irradiation.<sup>91</sup> These results demonstrate that flux synthesis is a worthwhile route for preparing highly crystalline perovskite oxynitrides.

Fig. 10(A) illustrates the anticipated growth mechanism of cubic-type  $\text{BaTaO}_2\text{N}$  particles showing how the flux-assisted nitridation conditions change the surface morphology of the resulting oxynitride. The following reaction steps are based on the XRD results:<sup>92</sup>



First,  $\text{BaCO}_3$  as the Ba precursor is decomposed to BaO, after which BaO and  $\text{Ta}_2\text{O}_5$  as the Ta source are dissolved in the KCl flux at a high temperature. The diffusion of the reactants through the molten flux leads to nucleation and growth of

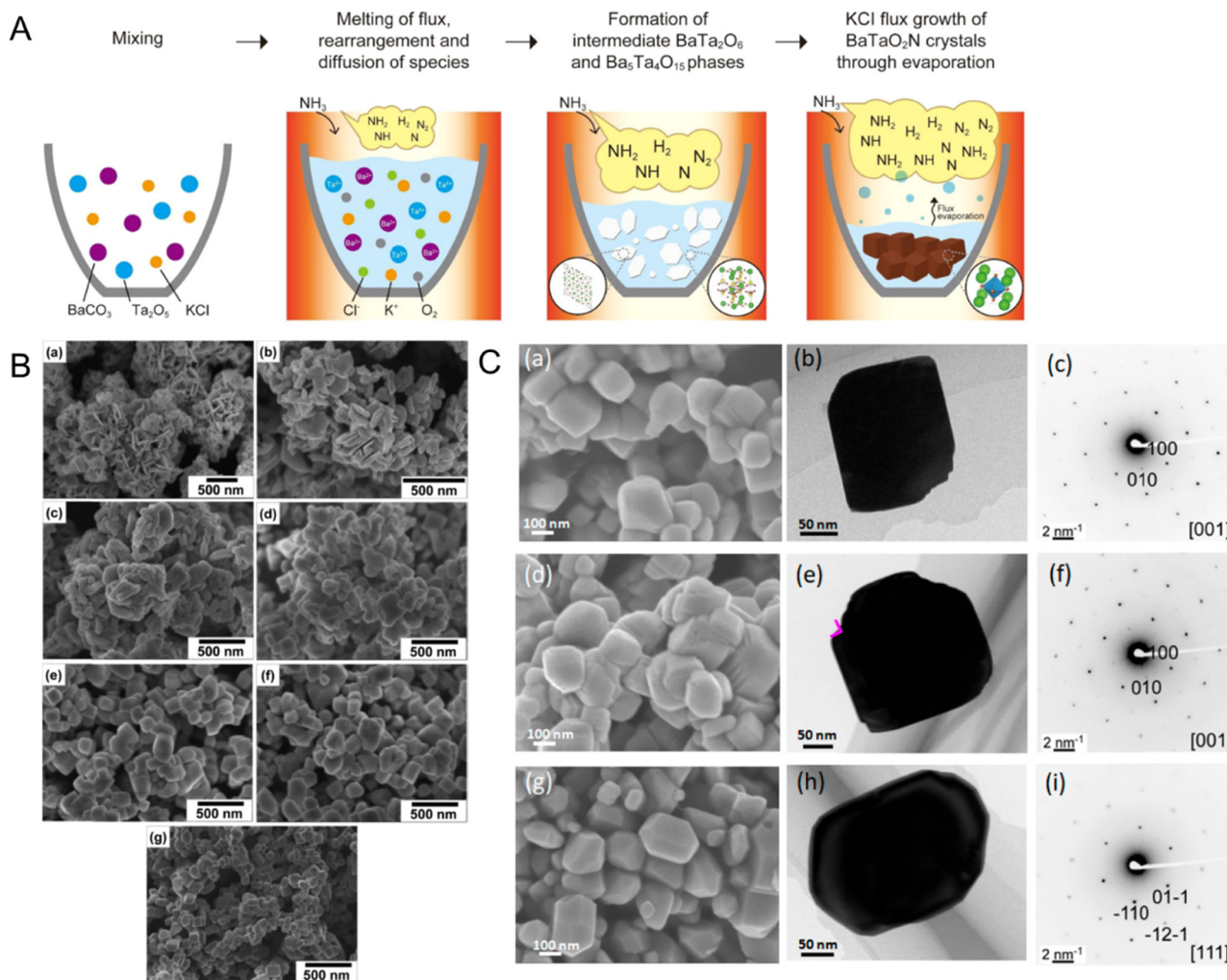


**Fig. 10** Flux-assisted nitridation. (A) A schematic of the growth mechanism of cube-like  $\text{BaTaO}_2\text{N}$  crystals during nitridation using molten KCl. Reproduced with permission.<sup>92</sup> Copyright 2015, ACS. (B) SEM images of  $\text{BaTaO}_2\text{N}$  particles grown *via* nitridation using molten KCl at 1223 K for (a) 0, (b) 1, (c) 2, (d) 4, (e) 6, (f) 8, or (g) 10 h. Reproduced with permission.<sup>92</sup> Copyright 2015, ACS. (C) SEM images, TEM images, and SAED patterns of  $\text{BaTaO}_2\text{N}$  prepared *via* flux-assisted nitridation using different fluxes of (a)–(c) RbCl, (d)–(f) CsCl, and (g)–(i)  $\text{BaCl}_2$ . Reproduced with permission.<sup>103</sup> Copyright 2020, ACS.

plate-like  $\text{BaTa}_2\text{O}_6$  and  $\text{Ba}_5\text{Ta}_4\text{O}_{15}$  (eqn (11) and (12), respectively). Finally, nitridation of the crystalline oxides under  $\text{NH}_3$  flow causes the crystallization and growth of  $\text{BaTaO}_2\text{N}$  particles (eqn (13)). The crystalline growth during nitridation at 1123 K for 0 h (*i.e.*, as the temperature was rising) provided vertically aligned plate-like shapes (Fig. 10(B)) comprising a mixture of  $\text{BaTaO}_2\text{N}$ ,  $\text{Ba}_5\text{Ta}_4\text{O}_{15}$ ,  $\text{BaTa}_2\text{O}_6$ , and  $\text{Ta}_2\text{O}_5$ . The plate-like shapes became thicker and irregular with increasing nitridation time up to 4 h. After 6 h of nitridation, the irregular particles had completely turned into the intrinsic crystal shape of cubic  $\text{BaTaO}_2\text{N}$  with clear edges. Subsequently, after 10 h, the cubic-like  $\text{BaTaO}_2\text{N}$  particles displaying specific (100) and (110) facets were more homogeneously dispersed. Interestingly, the surface morphology of  $\text{BaTaO}_2\text{N}$  during nitridation with a different flux was dissimilar to that during the KCl-assisted nitridation (Fig. 10(C)).<sup>103</sup> As RbCl and CsCl were utilized in the latter process,  $\text{BaTaO}_2\text{N}$  particles maintained their cubic crystal

structure, although their edges were slightly truncated and the exposed facets were predominantly along the (100) plane. In particular, the  $\text{BaTaO}_2\text{N}$  crystals prepared using CsCl possessed many small steps at the edges of the cubic structure. Meanwhile, the oxynitride crystals prepared *via*  $\text{BaCl}_2$ -assisted nitridation had a tetradecahedral shape with exposed (111) and (100) facets. The various fluxes of cations changed the electrostatic forces between the precursor ions during the growth of  $\text{BaTaO}_2\text{N}$ , which thus determined the surface morphology and predominant crystal facets of the resulting oxynitride.

### 3.2. Photoelectrodes

**3.2.1. Particulate electrodes prepared *via* spin coating, electrophoretic deposition (EPD), and particle transfer methods.** Particulate powder-type perovskite and layered perovskite oxynitrides are typically synthesized *via* the nitridation of their starting precursors, as discussed previously. To prepare oxynitride



photoelectrodes for PEC artificial synthesis systems, the particulate powder must be deposited onto a conductive substrate such as F-doped tin oxide (FTO). To this end, oxynitride photoelectrodes have been fabricated *via* spin coating, EPD, and particle transfer methods.<sup>3</sup> Spin coating is a very facile and scalable method for loading particulate oxynitrides onto conductive substrates, which has been utilized for the deposition of thin films in various applications, including solar cells.<sup>105–107</sup> A suspension of the oxynitride blended with organic solvents is drop-cast on the substrate *via* a spin coater while controlling the rotation speed. The thickness of the resulting particulate film is easily controllable *via* the surface morphology of the particles, the dispersion degree of the suspension, and the rotation speed.<sup>106,108</sup> For instance, 2D SrNbO<sub>2</sub>N particles doped with Zr<sup>4+</sup> have been uniformly packed onto an FTO substrate to produce a layer with a thickness of 2.5 μm by spin coating, as shown in Fig. 11(A).<sup>105</sup> The semi-transparent oxynitride film showed a significant photocurrent density of 2.0 mA cm<sup>-2</sup> at 1.23 V<sub>RHE</sub> for water splitting under sunlight irradiation, thereby proving the feasibility of using the spin coating method to prepare water-splitting films. Meanwhile, EPD has become the most ubiquitous means of preparing photoanodes from particulate oxynitrides.<sup>9,95,109</sup> Fig. 11(B) presents a schematic diagram of the fabrication of an oxynitride photoanode *via* the EPD method. The oxynitride powder is dispersed in an organic solvent including ionized species (*e.g.*, I<sup>-</sup>), and two conductive electrodes are

immersed parallel in the suspension solution. The positively and negatively charged species are shifted to the oppositely charged electrode at an applied DC voltage *via* electrostatic attraction, and the oxynitride particles are commonly deposited on the negative electrode. The distance between the two electrodes, the concentration of the charged species, the applied voltage, the duration, and so on, can all be varied to tune the thickness and deposition density of the resulting oxynitride film. In fact, heat treatment with conductive binders to promote the transfer of photogenerated charges between multiple layers of particles and/or the substrate (called necking) is an important step in preparing photoanodes *via* EPD.<sup>61,95</sup> The water-splitting photocurrent density over a TaON photoanode has been notably increased by necking treatment of the photoanode using TiCl<sub>4</sub>.<sup>110</sup> Nevertheless, the water-splitting activity of the photoanodes prepared *via* EPD is limited due to many grain boundaries between the oxynitride particles in the multiple layers slowing the migration of photoexcited charges. It has been suggested that the particle transfer method (Fig. 11(C)) can overcome the latter disadvantage in multi-layered particulate oxynitride photoanodes.<sup>104</sup> The ohmic contact layer (typically a metal) with a thickness of a few hundred nanometers is first deposited onto the top layer of the oxynitride particles loaded on a glass substrate by using radio-frequency (RF) magnetron sputtering. A thicker Ti conductor layer (~5 μm) is then deposited on the ohmic contact layer *via* RF magnetron sputtering,

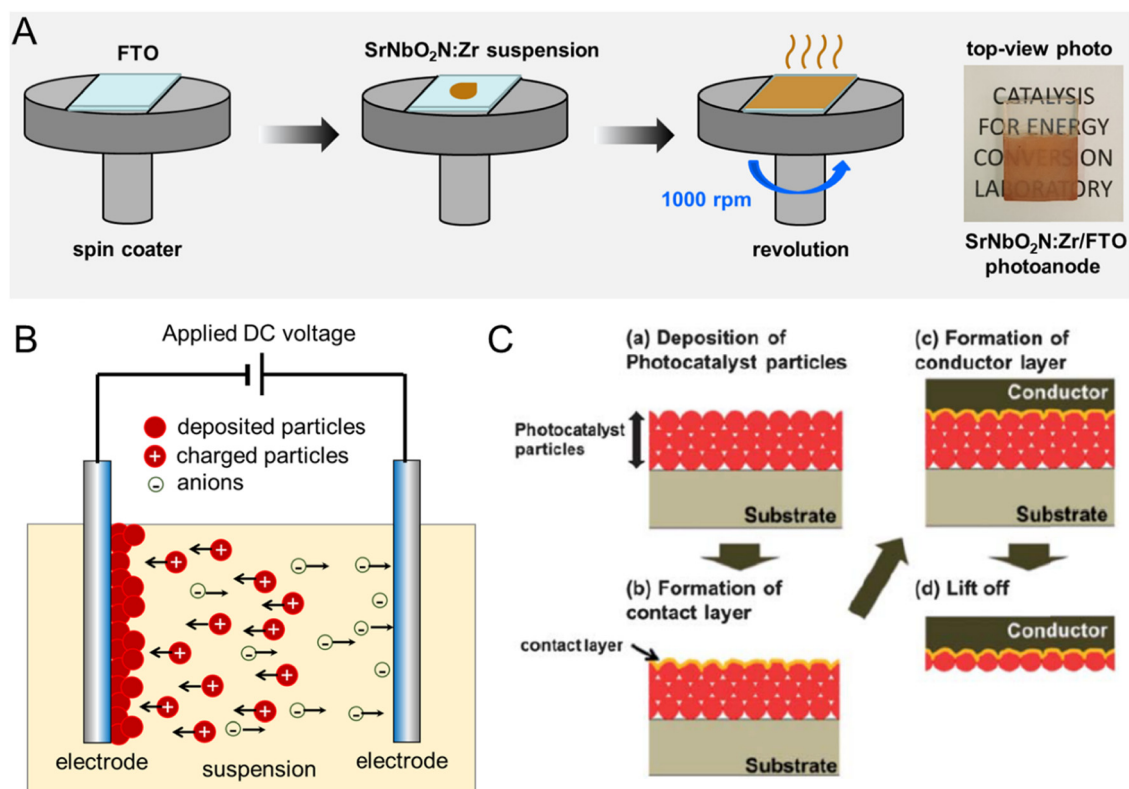


Fig. 11 Particulate photoelectrodes. Schematic diagrams of the preparation of perovskite oxynitride photoanodes *via* (A) spin coating, (B) electrodeposition (EPD), and (C) particle transfer methods. Reproduced with permission.<sup>104</sup> Copyright 2013, RSC. Reproduced with permission.<sup>105</sup> Copyright 2023, Elsevier.

resulting in high electroconductivity and mechanical strength. Subsequently, several of the upper layers physically connected to the conductor and contact layers are lifted off, which finally leads to an ideal oxynitride monolayer photoanode. An  $\text{LaTiO}_2\text{N}/\text{Ta}/\text{Ti}$  photoanode composed of a Ta ohmic contact and Ti conductive layers produced *via* the particle transfer method showed water-splitting photoactivity much higher than that of its counterpart prepared *via* EPD.<sup>104</sup> Moreover, the water-splitting photocurrent density at  $1.2 V_{\text{RHE}}$  of the  $\text{BaTaO}_2\text{N}/\text{Ta}/\text{Ti}$  photoanode was 10 times higher than that of previously reported photoanodes of the same material.<sup>61,62</sup> The oxynitride particles on the photoanodes prepared *via* the particle transfer method are well dispersed in a monolayer, which promotes the efficient separation and vertical transfer of charges photo-generated using a single oxynitride. In fact, the highest PEC activities of perovskite oxynitrides  $\text{LaTiO}_2\text{N}$ ,  $\text{BaTaO}_2\text{N}$ , and  $\text{BaNbO}_2\text{N}$  were observed in monolayered photoanode systems prepared *via* the particle transfer method.<sup>17-19</sup> These findings indicate that the monolayer electrode structure resulting from the particle transfer method is effective at controlling charge separation and transfer, thus enhancing the photoactivity for water splitting.

**3.2.2. Bottom-up fabrication.** The bottom-up fabrication of perovskite or layered perovskite oxynitride photoelectrodes from conductive substrates increases the conductivity of photo-generated charges between the oxynitride particles and/or the substrate over that of an electrode fabricated using the oxynitride powder, which probably enhances the photoreaction capability. Based on this, various bottom-up fabrication methodologies have been introduced for preparing oxynitride photoelectrodes.  $\text{LaTiO}_x\text{N}_y$  thin films grown on a TiN conductive layer have been synthesized by using a modified pulsed laser deposition method;<sup>111</sup> determining the surface crystal orientation of

the (001), (011), or (112) facets of the  $\text{LaTiO}_x\text{N}_y$  thin films was achieved by using different facet-oriented TiN conductive layers. However, the water-splitting activity of the resulting oxynitride film was very limited, mainly due to the non-stoichiometric composition of the anions in the oxynitride.  $\text{SrNbO}_2\text{N}$  crystals have been grown on an Nb substrate *via* flux coating  $\text{Sr}(\text{NO}_3)_2$  and chloride salts followed by nitridation.<sup>112</sup> The Sr-to-flux molar ratios and nitridation conditions determined the surface morphology and bulk crystallinity of the resulting  $\text{SrNbO}_2\text{N}$  and increased interfacial adhesion between  $\text{SrNbO}_2\text{N}$  and the Nb substrate. Despite the high interfacial adhesion of the oxynitride film, the water-splitting photoactivity was low. This was because the nitrogen during high-temperature nitridation managed to diffuse into the conductive substrate through the oxynitride semiconductor layer, which caused the generation of additional crystal and/or metallic interlayers. Thus, preparing photoactive oxynitride photoelectrodes *via* bottom-up fabrication is not straightforward.

Several studies showing the improved PEC water-splitting activity using perovskite oxynitrides prepared *via* bottom-up fabrication have recently been reported.<sup>52,113,114</sup> Fig. 12 presents top-view and cross-sectional SEM images of various bottom-up-fabricated oxynitride films. Vertical  $\text{SrNbO}_2\text{N}$  nanorod arrays have been grown on an Nb substrate *via* a hydrothermal method and subsequent nitridation.<sup>52</sup>  $\text{SrNbO}_x$  nanorod arrays were grown on the Nb substrate at a low temperature of 473 K, after which the oxide was transformed to  $\text{SrNbO}_2\text{N}$  nanorod arrays through nitridation at 1273 K for 2 h. As shown in Fig. 12(A), the diameter and length of the oxynitride nanorods were approximately 60 and 500 nm, respectively, thereby allowing favorable visible-light absorption and vertical separation of photogenerated charges. Interestingly, perovskite oxynitrides with 1D surface morphology have

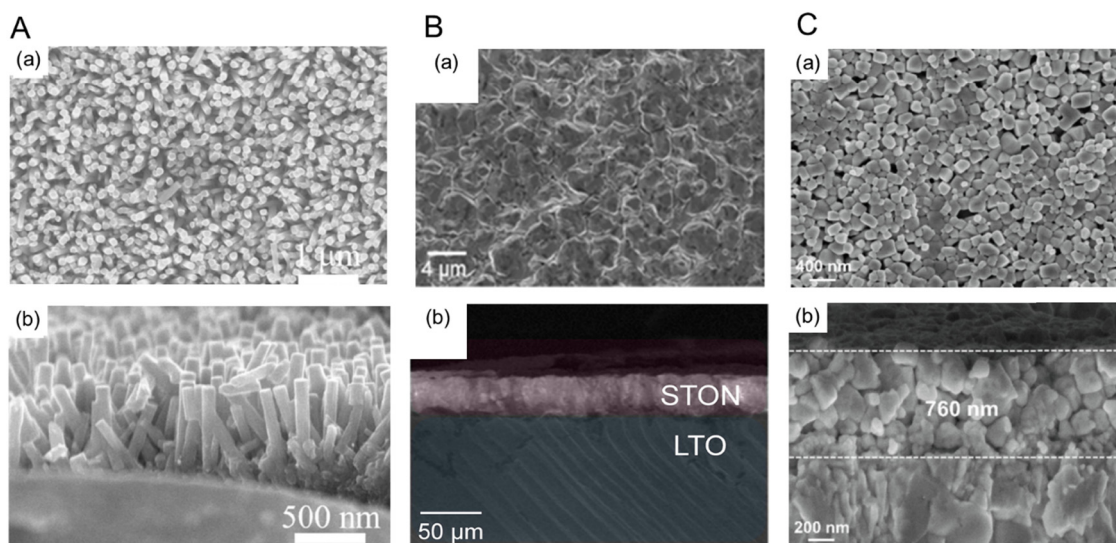


**Fig. 12** Bottom-up fabrication of perovskite oxynitride photoanodes. (a) Top-view and (b) cross-sectional SEM images of (A)  $\text{SrNbO}_2\text{N}$  nanorod arrays prepared *via* a hydrothermal method followed by nitridation, (B)  $\text{SrTaO}_2\text{N}$  crystals grown on a  $\text{LiTaO}_3$  substrate synthesized by using a reactive inorganic vapor method including nitridation, and (C)  $\text{BaTaO}_2\text{N}$  nanoparticle films deposited on a Nb substrate prepared *via* co-evaporation followed by nitridation. Reproduced with permission.<sup>52</sup> Copyright 2020, Wiley-VCH. Reproduced with permission.<sup>113,114</sup> Copyright 2022, Elsevier.

been reported for the first time. After the loading of  $\text{CoO}_x$  nanoparticles,  $\text{SrNbO}_2\text{N}$  nanorod arrays produced a notable photocurrent density of  $1.3 \text{ mA cm}^{-2}$  at  $1.23 V_{\text{RHE}}$  in an aqueous electrolyte at pH 13 under AM 1.5G simulated sunlight. Although the synthesis of the starting oxide at low temperature and a short nitridation period caused no additional interlayers detrimental to photoreactions, the light absorption edge of the  $\text{SrNbO}_2\text{N}$  nanorod arrays was approximately 630 nm, which is significantly shorter than 700 nm reported previously.<sup>15,93</sup>

Centimeter-scale perovskite  $\text{SrTaO}_2\text{N}$  crystals have been prepared by using a reactive inorganic vapor method including nitridation.<sup>114</sup> The oxynitride crystals were epitaxially grown on a (110)-oriented  $\text{LiTaO}_3$  substrate *via* the evaporation of Sr sources under an  $\text{NH}_3$  atmosphere. During the evaporation step,  $\text{Sr}^{2+}$  was exchanged with  $\text{Li}^+$  in the (110)-oriented  $\text{LiTaO}_3$  and nitrogen diffused into the oxide substrate simultaneously, leading to the growth of the  $\text{SrTaO}_2\text{N}$  crystals. Interestingly, different crystal orientations of  $\text{LiTaO}_3$  (*i.e.*, the (110) and (001) facets) resulted in nitridation rather than the intercalation of  $\text{Sr}^{2+}$  because the sizes of the lattice voids in the (110) and (001) facets are not large enough for the insertion of  $\text{Sr}^{2+}$  in the oxide substrate whereas they are in the (100) orientation. As shown in Fig. 12(B), the epitaxial growth of the perovskite  $\text{SrTaO}_2\text{N}$  crystals produced a dense film several tens of micrometers thick because of lattice expansion resulting from the insertion of  $\text{Sr}^{2+}$ . The dense film layer minimized inter-particle interfaces and grain boundaries, thereby resulting in a high photocurrent density of  $1.20 \text{ mA cm}^{-2}$  at  $0.6 V_{\text{RHE}}$  (with a low onset potential of  $0.35 V_{\text{RHE}}$ ) for water splitting in a 1 M NaOH electrolyte at pH 13.6. However, lattice expansion during the conversion to oxynitride caused the limited diffusion of  $\text{Sr}^{2+}$ , so the oxide substrate was not completely transformed to  $\text{SrNbO}_2\text{N}$ . Thus, these results indicate that the suitable selection of both the starting substrate and its crystal orientation is critical for the epitaxial growth of perovskite oxynitrides.

A co-evaporation method followed by nitridation to prepare a  $\text{BaTaO}_2\text{N}$  nanoparticle film directly grown on an Nb substrate has been reported.<sup>113</sup>  $\text{BaF}_2$  and  $\text{Ta}_2\text{O}_5$  precursors were uniformly evaporated onto the substrate *via* electron beam deposition and then completely transformed to  $\text{BaTaO}_2\text{N}$  *via* nitridation under an  $\text{NH}_3$  atmosphere. The resulting  $\sim 760$  nm-thick  $\text{BaTaO}_2\text{N}$  film comprised nanosized cubic crystalline particles, as shown in Fig. 12(C). The high crystallinity of the oxynitride was due to the uniform dispersion of Ba and Ta atoms in the resulting film. As a result, the  $\text{BaTaO}_2\text{N}$  photoanode produced a high photocurrent density of  $4.7 \text{ mA cm}^{-2}$  at  $1.23 V_{\text{RHE}}$  for water splitting in a 1 M KOH electrolyte at pH 13.6 under sunlight irradiation. The advantage of the co-evaporation method is the ability to regulate the reduction of  $\text{Ta}^{5+}$  during high-temperature nitridation by tuning the Ba/Ta ratio, which is similar to powder syntheses. In conclusion, the various bottom-up fabrication methods for perovskite oxynitrides reviewed in this article could enhance water-splitting activity by suppressing the generation of defects and additional interlayers in the resulting oxynitride film.

## 4. Bulk and surface engineering

### 4.1. Cation doping and substitution

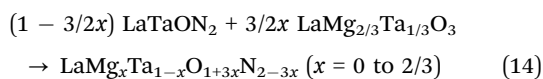
The doping (or substitution) of foreign elements into a semiconductor is a typical means of modifying its bulk and/or surface properties, which can lead to enhanced photocatalytic or PEC water-splitting activities. In this review, doping and substitution are distinguished from each other according to the amount of the alternative species introduced into the perovskite oxynitride: doping is below 10 at% and substitution is above 10 at%. Moreover, we cover the doping (or substitution) of the A- and/or B-site cations in the perovskite or layer perovskite oxynitrides. Perovskite  $\text{BaBO}_2\text{N}$  (B = Ta, Nb) has an ideal cubic crystal structure and the volume of its unit cells is markedly small.<sup>90,115</sup> By contrast, the cubic lattices of  $\text{AB}(\text{O},\text{N})_3$  (A = La, Ca, or Sr; B = Ta, Nb) are distorted because of the A-site cations being smaller than  $\text{Ba}^{2+}$  and the tilting of  $\text{B}(\text{O},\text{N})_6$  octahedra. These findings imply that the isostructural replacement of cations in perovskite oxynitrides with alternative ones could be significantly limited in terms of the size and amount of the dopant (or substituent).

The doping of perovskite  $\text{SrNbO}_2\text{N}$  with 2 at%  $\text{Zr}^{4+}$  reduced the bulk and surface defect densities of the oxynitride by suppressing the reduction of  $\text{Nb}^{5+}$  during nitridation, thereby improving its PEC water-splitting activity.<sup>105</sup> Although the limited replacement of  $\text{Nb}^{5+}$  with  $\text{Zr}^{4+}$  maintained the optical properties of the oxynitride (*i.e.*, the absorption of visible light up to a wavelength of 680 nm), using a larger amount of  $\text{Zr}^{4+}$  caused Zr-related impurity phases, thereby notably decreasing the photoactivity. Moreover, doping the  $\text{Nb}^{5+}$  sites in  $\text{BaNbO}_2\text{N}$  with  $\text{Ti}^{4+}$ ,  $\text{Zr}^{4+}$ ,  $\text{W}^{6+}$ , or  $\text{Mo}^{6+}$  has been attempted to control the donor density in the oxynitride bulk originating from the generation of reduced species during nitridation.<sup>116</sup> Doping with lower-valent cations  $\text{Ti}^{4+}$  and  $\text{Zr}^{4+}$  suppressed the generation of  $\text{Nb}^{4+}$  during nitridation whereas doping with higher-valent cations  $\text{W}^{6+}$  and  $\text{Mo}^{6+}$  rather increased the donor density. Moreover, doping with up to 4 at%  $\text{Ti}^{4+}$  resulted in the synthesis of  $\text{BaNbO}_2\text{N}$  without impurity traces, which thus exhibited the highest water-splitting activity. However, doping of the lower-valent cations at the Ta-sites in  $\text{BaTaO}_2\text{N}$  did not effectively lower the defect density and thus improve photoactivity despite the similarity of the ionic radii of 6-coordinate  $\text{Ta}^{5+}$  (78 pm) and 6-coordinate  $\text{Nb}^{5+}$  (78 pm). Selective replacement at the Ta-site in perovskite  $\text{BaTaO}_2\text{N}$  using 5 at%  $\text{Al}^{3+}$ ,  $\text{Ga}^{3+}$ ,  $\text{Sc}^{3+}$ , or  $\text{Zr}^{4+}$  for improving photocatalytic HER and OER activity has also been considered.<sup>117</sup> In particular, the doping of  $\text{BaTaO}_2\text{N}$  with  $\text{Mg}^{2+}$  or  $\text{Zr}^{4+}$  enhanced OER photoactivity in a sacrificial reagent by modifying the optoelectronic and surface properties of the oxynitride. Therefore, limited doping of  $\text{AB}(\text{O},\text{N})_3$  using alternative cations alters the surface properties of oxynitrides (such as defect and donor densities) while maintaining their bulk properties (such as the crystalline structure and optical properties).

Co-substitution of the  $\text{Ta}^{5+}$  site of  $\text{Ta}_3\text{N}_5$  with 33 at% 6-coordinate  $\text{Mg}^{2+}$  (86 pm) and  $\text{Zr}^{4+}$  (86 pm) led to significant improvement in the anodic photocurrent density and onset potential for PEC water splitting.<sup>118</sup> This large amount of



substitution modified not only the band structure but also the surface morphology of the original  $\text{Ta}_3\text{N}_5$ . The difference in valence between parent  $\text{Ta}^{5+}$  and alternative cations  $\text{Mg}^{2+}$  and  $\text{Zr}^{4+}$  caused additional  $\text{N}^{3-}/\text{O}^{2-}$  replacement to replenish the charge imbalance. Increasing and decreasing the concentration of  $\text{Mg}^{2+}/\text{Zr}^{4+}$  cations and  $\text{N}^{3-}$  anions respectively shifted the CBM and VBM potentials negatively from those of parent  $\text{Ta}_3\text{N}_5$ . This strategy was also applied in the synthesis of perovskite  $\text{LaMg}_x\text{B}_{1-x}\text{O}_{1+3x}\text{N}_{2-3x}$  ( $\text{B} = \text{Ta}, \text{Nb}; x = 0$  to  $2/3$ ) solid solutions, leading to overall water-splitting activity *via* one-step photoexcitation.<sup>41,42</sup> Fig. 13(A)-(a) portrays the crystal structures of  $\text{LaMg}_x\text{Ta}_{1-x}\text{O}_{1+3x}\text{N}_{2-3x}$  solid solutions after substituting  $\text{Ta}^{5+}$  with  $\text{Mg}^{2+}$ .<sup>41</sup> The general formula of these perovskite oxynitrides is given by



The composition of the  $\text{LaMg}_x\text{Ta}_{1-x}\text{O}_{1+3x}\text{N}_{2-3x}$  solid solutions was easily modified by mixing perovskite oxynitride  $\text{LaTaON}_2$  and perovskite oxide  $\text{LaMg}_{2/3}\text{Ta}_{1/3}\text{O}_3$  at the atomic level. The significant substitution of  $\text{Mg}^{2+}$  in  $\text{LaTaON}_2$  was realized after the nitridation of the starting oxides blended at the atomic level *via* a polymerized-complex method. The greater the level of substitution of  $\text{Ta}^{5+}$  with  $\text{Mg}^{2+}$ , the greater the increase in the composition

ratio of  $\text{LaMg}_{2/3}\text{Ta}_{1/3}\text{O}_3$ , resulting in a marked change in the optical properties of the resulting oxynitrides (Fig. 13(A)-(b)). The wavelength of the light absorption edge of  $\text{LaMg}_x\text{Ta}_{1-x}\text{O}_{1+3x}\text{N}_{2-3x}$  blue-shifted gradually from 640 nm (pure  $\text{LaTaON}_2$ ) to 270 nm (fully substituted  $\text{LaMg}_{2/3}\text{Ta}_{1/3}\text{O}_3$ ).

This phenomenon was also observed in the substitution of  $\text{Nb}^{5+}$  with  $\text{Mg}^{2+}$  in counterpart  $\text{LaNbON}_2$ .<sup>42</sup> Fig. 13(B)-(a) presents UV-vis DRS spectra of  $\text{LaMg}_x\text{Nb}_{1-x}\text{O}_{1+3x}\text{N}_{2-3x}$  ( $x = 0$  to  $2/3$ ) showing a gradual blue-shift of the absorption onset wavelengths from 700 to 320 nm. In addition to the increase in the  $E_g$ , the CBM and VBM potentials of the solid solutions also shifted to the negative and positive sides, respectively, as portrayed in Fig. 13(B)-(b). The band structure diagrams of the solid solution series demonstrate that the substitution of  $\text{Nb}^{5+}$  with  $\text{Mg}^{2+}$  in  $\text{LaNbON}_2$  not only increases the concentration of the O 2p atomic orbital (leading to the positive shift of the VBM) but also decreases the concentration of the Nb 4d orbital (causing the negative shift of the CBM). The substitution of  $\text{Mg}^{2+}$  largely reduced the bulk and surface defect densities of  $\text{LaMg}_x\text{Nb}_{1-x}\text{O}_{1+3x}\text{N}_{2-3x}$  solid solutions, which is similar to the effect of the small-cation doping of oxynitrides. Moreover, the subsequent changes in the optical properties (*i.e.*, the  $E_g$  value and band structure) of the oxynitrides were significant. In addition, surface modification using cocatalysts finally activated the overall water-splitting capability of  $\text{LaMg}_x\text{B}_{1-x}\text{O}_{1+3x}\text{N}_{2-3x}$ ,

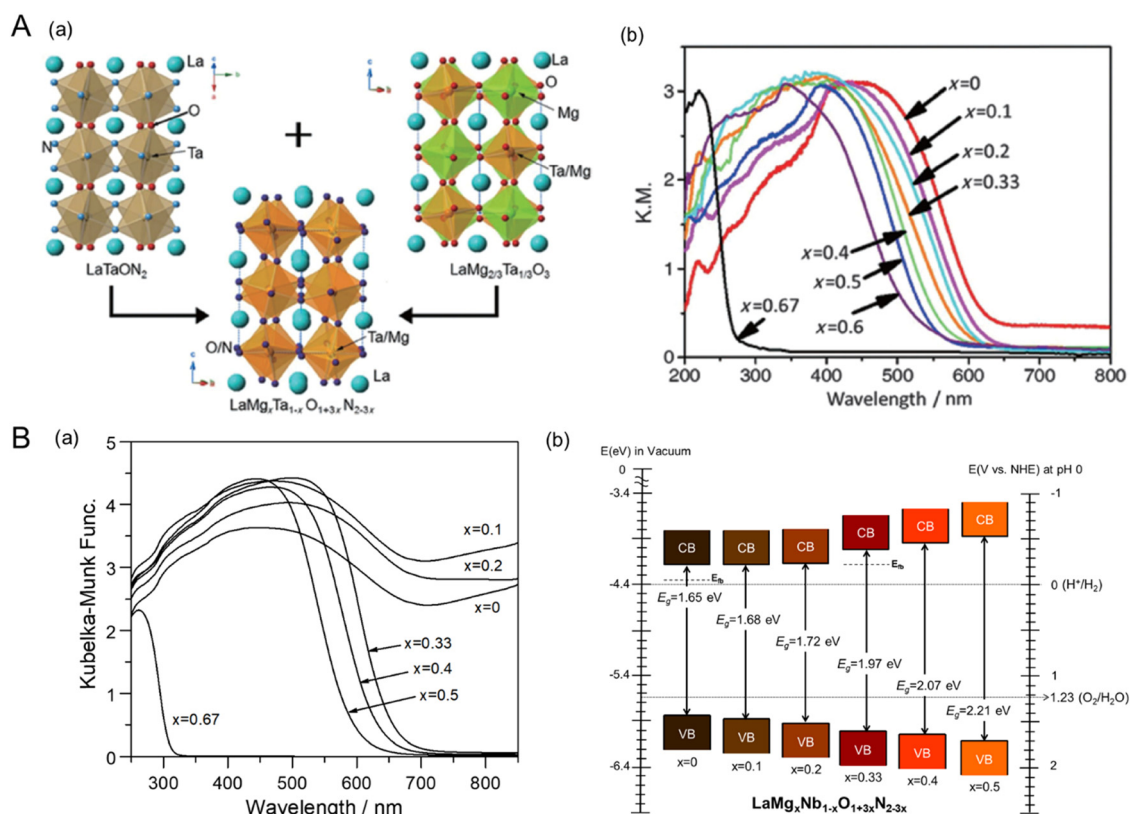


**Fig. 13** Substitution of  $\text{B}^{5+}$  with  $\text{Mg}^{2+}$  in perovskite  $\text{LaBON}_2$  ( $\text{B} = \text{Ta}, \text{Nb}$ ). (A) (a) Crystalline structure and (b) UV-vis DRS spectra of the  $\text{LaMg}_x\text{Ta}_{1-x}\text{O}_{1+3x}\text{N}_{2-3x}$  ( $x = 0$  to  $2/3$ ) powder after replacing some of the  $\text{Ta}^{5+}$  with  $\text{Mg}^{2+}$ . Reproduced with permission.<sup>41</sup> Copyright 2015, Wiley-VCH. (B) (a) UV-vis DRS spectra and (b) band structure diagrams of  $\text{LaMg}_x\text{Nb}_{1-x}\text{O}_{1+3x}\text{N}_{2-3x}$  ( $x = 0$  to  $2/3$ ) after replacing some of the  $\text{Nb}^{5+}$  with  $\text{Mg}^{2+}$ . Reproduced with permission.<sup>42</sup> Copyright 2021, RSC.

thereby producing stoichiometric H<sub>2</sub> and O<sub>2</sub> evolution. Interestingly, the highest gas evolution rates for water-splitting were achieved using LaMg<sub>1/3</sub>B<sub>2/3</sub>O<sub>2</sub>N (*i.e.*,  $x = 1/3$ ) irrespective of the cationic occupancy of the B sites in the oxynitride. As a result, the visible-light-driven overall water-splitting activity is mainly attributed to the expanded bandgap enabling a photoresponse of up to 600 and 650 nm for LaMg<sub>1/3</sub>Ta<sub>2/3</sub>O<sub>2</sub>N and LaMg<sub>1/3</sub>Nb<sub>2/3</sub>O<sub>2</sub>N, respectively. Likewise, the bulk modification of oxynitrides *via* substitution with alternative cations has been subsequently applied: Zn<sup>2+</sup> for Ta<sup>5+</sup> in perovskite BaTaO<sub>2</sub>N,<sup>119</sup> Zr<sup>4+</sup> for Ta<sup>5+</sup> in LaTaON<sub>2</sub>,<sup>120</sup> Mg<sup>2+</sup> for Ti<sup>4+</sup> in LaTiO<sub>2</sub>N,<sup>121</sup> La<sup>3+</sup> for Ti<sup>4+</sup> in layered perovskite Sr<sub>2</sub>TiO<sub>4</sub>,<sup>122</sup> and so on. All these outcomes obviously demonstrate that the substitution of the B sites in oxynitrides with alternative cations is a very useful way of modifying the bulk properties of the parent oxynitride and thus improving the latter's photocatalytic water-splitting capability.

#### 4.2. Varying the surface morphology

The electrochemical activity of an electrocatalyst (*e.g.*, Pt nanoparticles) for oxidation and reduction reactions is typically

proportional to its electrochemically active surface area containing its reaction sites for accessing the electrolyte.<sup>124–127</sup> The surface morphology (including the particle size and shape) of the electrocatalyst to increase reaction sites is thus critical for progressing electrochemical reactions efficiently. In contrast, the surface morphology of a semiconductor influences visible-light harvesting, the reaction efficiency of photocarriers, and the deposition coverage of cocatalysts (*e.g.*, CoO<sub>x</sub>) on which the actual photoreaction takes place. Because the small size of semiconductor particles can lead to a short diffusion distance for the photogenerated charges, it increases the charge separation, transfer, and collection efficiencies, thereby enhancing photoactivity.<sup>128</sup> BaNbO<sub>2</sub>N particles of various sizes prepared *via* the nitridation of Ba<sub>5</sub>Nb<sub>4</sub>O<sub>15</sub> size-controlled in the range from 0.2 to 50 μm exhibit photocatalytic water oxidation activity depending on the particle size in an aqueous electrolyte including a sacrificial reagent.<sup>129</sup> Similarly, small scheelite-type LaNbO<sub>4</sub> particles as the starting oxide produced small LaNbON<sub>2</sub> particles with fewer defects after nitridation with significantly high photocatalytic water oxidation activity under visible-light Xe lamp

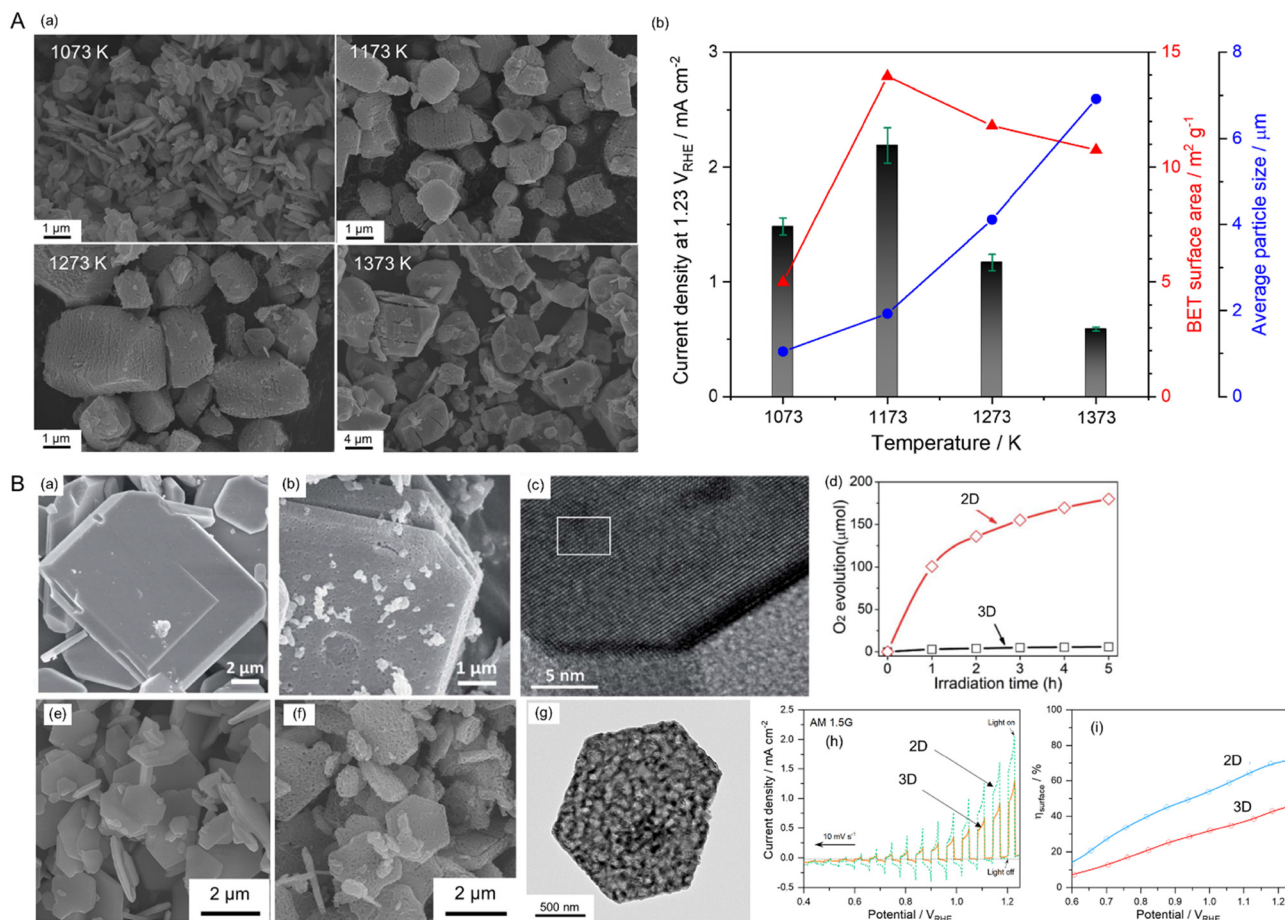


**Fig. 14** Varying the surface morphology of Nb-based perovskite oxynitrides. (A) SEM images (a) and the corresponding PEC water-splitting activity (b) of BaNbO<sub>2</sub>N particles of various sizes. Reproduced with permission.<sup>88</sup> Copyright 2022, Elsevier. (B) SEM images of starting LaKNaNbO<sub>5</sub> (a) and the corresponding 2D LaNbON<sub>2</sub> (b) after nitridation along with an HRTEM image (c) and the photocatalytic O<sub>2</sub> evolution activity (d) of the 2D oxynitride particles. Reproduced with permission.<sup>123</sup> Copyright 2020, RSC. SEM images of starting Sr<sub>5</sub>Nb<sub>4</sub>O<sub>15</sub> (e) and the resulting 2D SrNbO<sub>2</sub>N (f) after nitridation along with an HRTEM image (g) and the PEC water-splitting activity (h) and charge separation efficiency (i) of the 2D oxynitride photoanode. The photoactivities of both 2D oxynitrides were compared with those of typical 3D oxynitrides. Reproduced with permission.<sup>105</sup> Copyright 2023, Elsevier.

irradiation ( $\lambda > 420$  nm).<sup>94,95</sup> Fig. 14(A) presents the size dependence of perovskite BaNbO<sub>2</sub>N particles on PEC water-splitting activity.<sup>88</sup> The size of the oxynitride particles was systematically tuned *via* the nitridation of Ba<sub>5</sub>Nb<sub>4</sub>O<sub>15</sub> with various average sizes (1.05, 1.93, 4.11, or 6.92  $\mu\text{m}$ ). The oxide particles synthesized *via* a polymerized-complex method were gradually grown by increasing the calcination temperature from 1073 to 1373 K. Their conversions to the corresponding oxynitride exclusively increased the surface porosity without an increase in particle size, except for the nitridation of the oxide calcined at 1073 K. The small, porous oxynitride prepared from the oxide *via* calcination at 1173 K provided both the largest BET and electrochemical surface areas, resulting in the highest photocurrent density of 2.2 mA cm<sup>-2</sup> at 1.23 V<sub>RHE</sub> for sunlight-driven water splitting. The photocurrent decreased upon increasing the oxynitride particle size. Although the smallest non-porous BaNbO<sub>2</sub>N particles prepared *via* nitridation of the oxide calcined at 1073 K were highly crystalline, this did not contribute to increasing the surface reaction sites. This result demonstrates that the size reduction of oxynitride particles accompanied by an increase in the surface reaction area clearly enhances the water-splitting photoactivity. In fact, the photon flux in the solar spectrum (used to determine the number of charges generated during photoreactions) is constant depending on the light wavelength. Therefore, the activity result of perovskite BaNbO<sub>2</sub>N depending on its particle size implies that the photo-response of the oxynitride is still relatively poor, and there is a large room for improvement in the activity up to the theoretical maximum STH efficiency of each oxynitride.

Besides the particle size, the surface shape of a perovskite or layered perovskite oxynitride also influences its photoactivity. As discussed previously, fluxes during nitridation can be used to readily change the shape of the oxynitride particles. The employment of different fluxes during nitridation and/or calcination of the starting oxide has been applied to vary the shape and size of 3D SrNbO<sub>2</sub>N particles.<sup>93</sup> Moreover, the nitridation of La<sub>2</sub>Ti<sub>2</sub>O<sub>7</sub> using an NaCl–KCl flux produced highly porous brick-like LaTiO<sub>2</sub>N particles.<sup>16</sup> The surface shape of the oxynitride with a large surface area improved its photocatalytic water oxidation activity because of the high dispersion of CoO<sub>x</sub> or IrO<sub>2</sub> cocatalysts over the large surface of the oxynitride. Meanwhile, rarely reported vertical SrNbO<sub>2</sub>N nanorod arrays (as discussed earlier) with a 1D structure of the semiconductor promoted the strong separation of photogenerated charges exclusively in the vertical direction, thereby enhancing PEC activity.

Over the past few years, newly emerged 2D configurations of perovskite and layered perovskite oxynitrides have been found to provide a short diffusion transfer route for the photoexcited charges and thus lower their recombination.<sup>31,130–133</sup> The electrons and holes photogenerated in HCa<sub>2</sub>Nb<sub>3</sub>O<sub>10</sub> nanosheets and selectively transferred to the surface of 2D Ca<sub>2</sub>Nb<sub>3</sub>O<sub>10</sub><sup>-</sup> plates without their self-recombination significantly improved photocatalytic water reduction activity under UV irradiation ( $\lambda > 300$  nm).<sup>134</sup> A 2D layered perovskite K<sub>2</sub>LaTa<sub>2</sub>O<sub>6</sub>N was also stably active during the same photoreaction under visible-light illumination ( $\lambda > 400$  nm).<sup>89</sup> The optical and electrical

properties and charge transport of 2D RP-type A<sub>2</sub>BO<sub>3</sub>N (A = Ca, Sr, or Ba; B = Ta or Nb) layered perovskites have been studied based on density functional theory.<sup>135</sup> Thereby, the mobility of the electrons (or holes) photogenerated in the 2D layered perovskites was found to be much quicker than in the 3D perovskites. These results indicate that the advantages of 2D morphology (*i.e.*, the fast vertical charge transfer to the surface of the oxynitride plates) enhance water-splitting photoactivity.

Because the crystal structure of perovskite AB(O,N)<sub>3</sub> is cubic, the 3D shape of the oxynitride is typically synthesized. However, 2D-type starting oxides with a layered perovskite structure could be transformed into 2D oxynitrides capable of absorbing visible light. Fig. 14(B) shows the surface morphologies of the starting oxides and their corresponding oxynitrides, along with the visible-light-driven photoactivity of the 2D oxynitrides compared with the corresponding 3D type. In the upper row, it can be seen that the smooth layered LaKNaNbO<sub>5</sub> plates were converted to porous 2D LaNbON<sub>2</sub> *via* nitridation accompanied by volatilization of the K and Na species.<sup>123</sup> This conversion also worked well in the synthesis of counterpart LaTaON<sub>2</sub> using LaKNaTaO<sub>5</sub>.<sup>131</sup> Interestingly, volatilization of the layered oxide along the [001] direction resulted in the shape of the oxynitride with exposed (010) surface facets remaining unchanged. The photocatalytic water oxidation activity of 2D LaNbON<sub>2</sub> with (010) facets was much higher than that of conventional 3D LaNbON<sub>2</sub> with mostly (100) facets. The efficient transfer of charges along the (010) facets of the 2D oxynitride and its low defect density resulting from the fast nitridation and the volatilization of the K and Na species led to its enhanced photoactivity. Meanwhile, layered perovskite Zr-doped Sr<sub>5</sub>Nb<sub>4</sub>O<sub>15</sub> with a 2D-type truncated octahedral structure was completely transformed to porous 2D-type SrNbO<sub>2</sub>N particles with an identical morphology, as shown in the bottom row of Fig. 14(B).<sup>105</sup> The conversion process yielded oxynitrides with fewer defects, as discussed in detail in the earlier synthesis section using A-site cation-rich starting oxides. The 2D shape of the SrNbO<sub>2</sub>N particles, as well as their high crystallinity, significantly heightened the PEC water-splitting activity of the oxynitride. The efficiency of charge separation by the 2D SrNbO<sub>2</sub>N was much higher than that by the conventional 3D oxynitride. Moreover, the charge transfer resistance in the 2D oxynitride was relatively low. These results enable us to draw the same conclusion that oxynitrides with a 2D surface structure facilitate strong charge separation and fast transfer of charges photogenerated during water splitting.

### 4.3. Controlling the crystallographic facets

Crystal facet engineering for more efficient photoreaction activity by effectively promoting the preferential separation of charges between two adjacent anisotropic facets in a semiconductor during the reaction has been recently reported.<sup>27,136</sup> Representatively, it has been demonstrated that monoclinic BiVO<sub>4</sub> particles with two different facets prepared *via* a hydrothermal method and the selective photo-deposition of cocatalysts could separate photogenerated holes in the (110) facets while collecting the counterpart electrons in the (010) facets.<sup>137</sup> Au, Pt, or Ag



nanoparticles were deposited on the (010) facets of  $\text{BiVO}_4$  under light irradiation while  $\text{MnO}_x$  or  $\text{PbO}_2$  particles were coated on the (110) facets of the oxide in the same manner. Both selective depositions of the cocatalysts, particularly the Pt and  $\text{MnO}_x$  particles, dramatically enhanced the photocatalytic water oxidation activity of the  $\text{BiVO}_4$  particles. Similarly, spatial separation of the photogenerated holes and electrons with  $\text{CoO}_x$  and  $\text{RhO}_x$  cocatalysts, respectively, also improved the PEC water oxidation activity.<sup>138</sup> Moreover, optoelectrical simulation proved that facet engineering increased the efficiencies of not only charge

injection but also charge separation during the water oxidation reaction.

The facet engineering of cubic perovskite  $\text{SrTiO}_3\text{:Al}$  was very effective at spatially separating the photogenerated charges to two different facets, thus driving overall water splitting *via* one-step photoexcitation.<sup>12</sup>  $\text{Rh/Cr}_2\text{O}_3$  as an HER cocatalyst and  $\text{CoOOH}$  as an OER catalyst were sequentially photo-deposited onto the electron-attracting (100) facets and the hole-collecting (110) facets, respectively. The resulting anisotropic charge transport achieved high overall water-splitting activity that

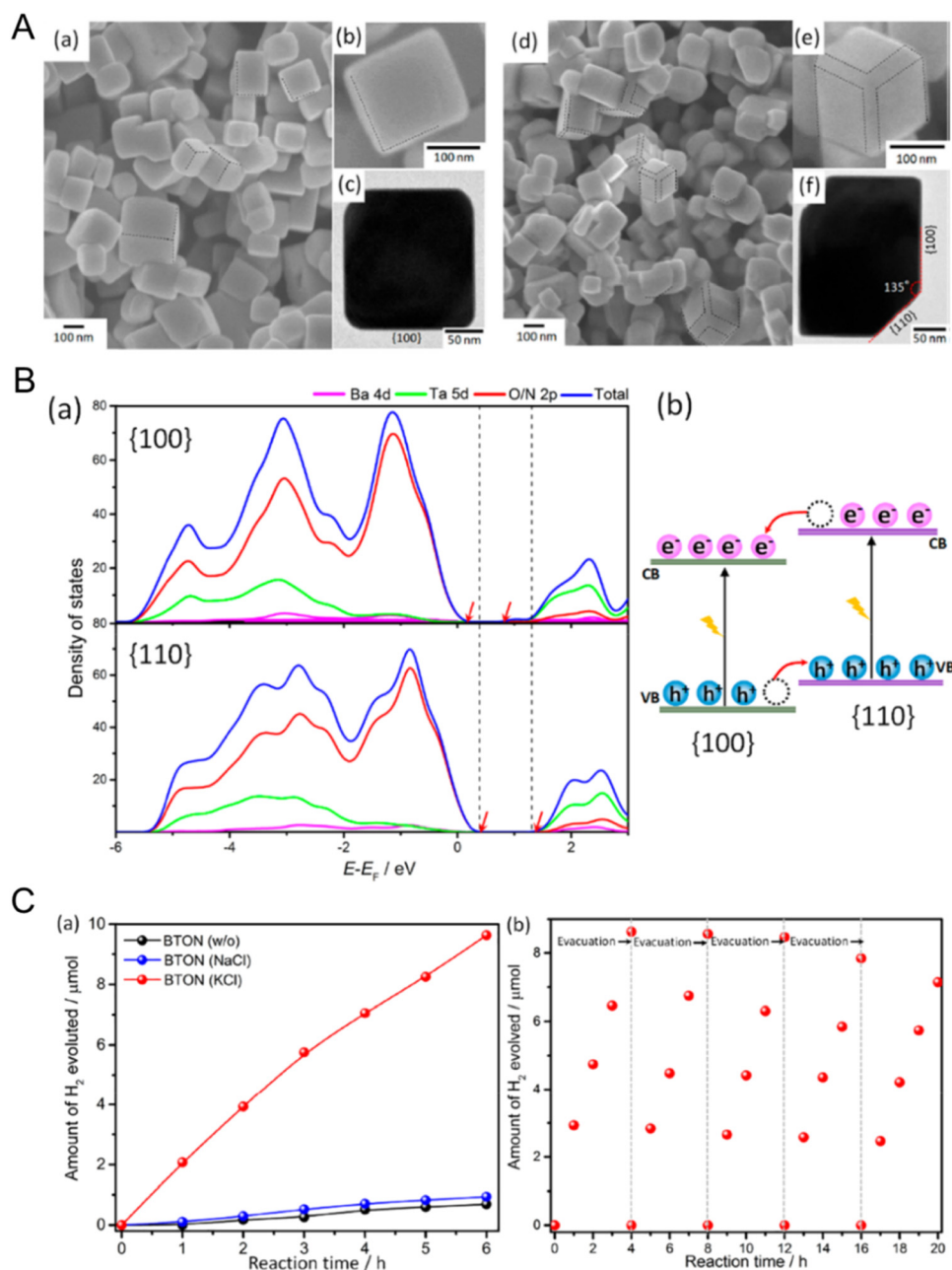


**Fig. 15** Crystal facet engineering of perovskite and layered perovskite oxynitrides. (A) SEM and TEM images of  $\text{BaTaO}_2\text{N}$  particles prepared *via* flux-assisted nitridation using (a)–(c) NaCl and (d)–(f) KCl molten salts. (B) The density of states of the different energy levels of the (100) and (110) facets of  $\text{BaTaO}_2\text{N}$  prepared *via* KCl-assisted nitridation. (C) (a) Photocatalytic  $\text{H}_2$  evolution activity using the two different  $\text{BaTaO}_2\text{N}$  particles and (b) cyclic testing using the oxynitride particles prepared *via* KCl-assisted nitridation. Reproduced with permission.<sup>139</sup> Copyright 2019, ACS.

was almost consistent with the theoretical quantum efficiency of SrTiO<sub>3</sub>. Unlike the oxide, it is difficult to prepare perovskite oxynitrides with exposed crystal facets to spatially separate charges because their crystal growth is not easily controlled during typical high-temperature nitridation. Fortunately, flux-assisted nitridation may offer a feasible means of tuning the surface morphology of oxynitrides, as discussed in the synthesis section. Symmetric BaTaO<sub>2</sub>N particles with only the (100) and (110) facets exposed have been successfully prepared *via* flux-assisted nitridation, as displayed in Fig. 15(A).<sup>139</sup> The starting precursors of Ba and Ta were rearranged and then recrystallized in the molten salt during nitridation, which resulted in well-defined cubic BaTaO<sub>2</sub>N particles of approximately 200 nm in size. Interestingly, the BaTaO<sub>2</sub>N crystals prepared using a NaCl flux exhibited a cubic structure with six isotropic (100) facets whereas the oxynitride synthesized using a KCl flux presented a cubic-like structure with additional smooth (110) facets at the twelve corners of the (100) facets. The ionic species of fluxes become adsorbed on the crystal facets, thereby enabling faster growth and changes in the electrostatic interactions between the crystals. Because the ionic radius of six-coordinate K<sup>+</sup> (152 pm) is very similar to that of six-coordinate Ba<sup>2+</sup> (149 pm), K<sup>+</sup> can more easily occupy the Ba<sup>2+</sup> positions at the interface between BaTaO<sub>2</sub>N and KCl. This not only suppresses the crystal growth of BaTaO<sub>2</sub>N with the most stable (100) facets but also leads to the formation of secondary stable (110) facets. According to density functional theory calculations (Fig. 15(B)), the estimated surface energy of the (110) facets is higher than that of the (100) facets, meaning that the CBM and VBM potentials of the (110) facets are located

above those of the (100) facets. Thus, a facet junction is generated between the anisotropic (100) and (110) facets of a BaTaO<sub>2</sub>N particle, thereby boosting the selective transfer of photogenerated electrons and holes to the (100) and (110) facets, respectively. Like the previously described BiVO<sub>4</sub> system, Pt and MnO<sub>x</sub> particles were separately photo-deposited onto the (100) and (110) facets of BaTaO<sub>2</sub>N. As a result, the BaTaO<sub>2</sub>N crystals prepared using a KCl flux presented significantly improved water reduction activity compared with those using NaCl. Therefore, crystal facet engineering promoting selective separation and transfer of charges during photoreactions offers an effective strategy for enhancing the photoactivity of perovskite and layered perovskite oxynitrides by adjusting the crystal facets during their synthesis.

## 5. Conclusions and challenges

We discussed the preparation and use of perovskite AB(O,N)<sub>3</sub> and layered perovskite oxynitrides A<sub>n+1</sub>B<sub>n</sub>(O,N)<sub>3n+1</sub> as potential semiconductors for visible-light-driven artificial photosynthesis, as shown in Fig. 16. The materials are capable of absorbing visible light wavelengths up to 750 nm at most, and their band structures straddle the various redox potentials of the HER, OER, CER, H<sub>2</sub>O<sub>2</sub> production, and CO<sub>2</sub> reduction, among others. Moreover, they are chemically stable in aqueous media over a wide pH range where photoreactions can take place. They fulfill the thermodynamic requirements for various photocatalytic processes to generate renewable, eco-friendly, and/or high value-added products such as H<sub>2</sub> and NH<sub>3</sub> with high theoretical

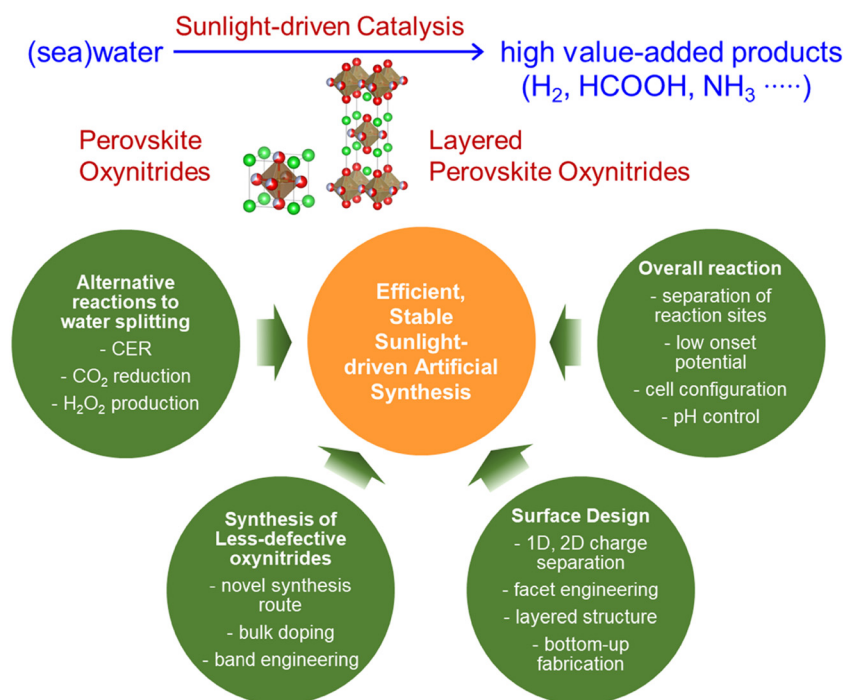


Fig. 16 Sunlight-driven catalysis and the challenges of perovskite and layered perovskite oxynitrides to artificially synthesize renewable, high value-added products such as H<sub>2</sub>.

solar-to-fuel energy conversion efficiency. Based on their favorable optical and chemical properties, perovskite and layered perovskite oxynitrides have been employed as both light absorbers and photocatalysts for visible-light-driven water splitting to produce H<sub>2</sub> over several decades. In addition, using them for CO<sub>2</sub> reduction and the CER as an alternative oxidation reaction to the OER to obtain high value-added products such as HCOOH have recently been reported. The adaption of the CER, feasible by using seawater instead of fresh water, not only boosted the oxidation kinetics but also enhanced the H<sub>2</sub> production activity in neutral electrolytes. However, the perovskite and layered perovskite oxynitrides have shown low photoactivity and long-term stability during various photoreactions, which are still far from the requirements for commercialization (corresponding to STH values of above 10%).

Because Ti<sup>4+</sup>, Ta<sup>5+</sup>, and Nb<sup>5+</sup> in the perovskite and layered perovskite oxynitrides are readily reduced during high-temperature nitridation, the surface and bulk properties of the latter can change due to the presence of defects and/or traces of impurities. Defects in perovskite and layered perovskite oxynitrides boost the recombination of photogenerated holes and electrons during photoreactions, thereby limiting their photoactivity. This phenomenon can be reduced by various synthesis strategies and surface and bulk engineering including doping and substitution. Moreover, photooxidation of the oxynitride surface, which results in the release of N<sub>2</sub> and a positive shift in the surface Fermi level, can be completely suppressed *via* surface modification to provide separated compartments for HER and OER cocatalysts or passivation layers.

Controlling the surface morphology of the oxynitride particles and/or electrodes can spatially separate the transfer orientation of photogenerated holes and electrons, thus leading to dramatic improvement in the sunlight-driven catalytic activity. Although 1D and 2D perovskite AB(O,N)<sub>3</sub> were rarely studied in terms of the synthesis method, the morphologically modified surfaces of the oxynitrides were found to largely increase the separation efficiency of charges generated during PEC water splitting. It is known that the surface shape of metal oxynitrides such as Ta<sub>3</sub>N<sub>5</sub> is relatively easy to be transformed even through high-temperature nitridation. However, it is difficult to prepare AB(O,N)<sub>3</sub> with 1D or 2D surface morphology because two different cations at A- and B-sites are typically sintered at the high temperature probably causing the change in the surface structure. Alternatively, the charges generated during photoreactions can be spatially separated by crystal facet engineering and the employment of layered perovskite oxynitrides. The crystal facet engineering of BaTaO<sub>2</sub>N, materialized by flux-assisted nitridation including a recrystallization stage, proved that (100) and (110) facets play roles as electron-attracting and hole-collecting sites, respectively. The layered perovskite oxynitrides with a 2D crystal structure, which allow selective transfer of holes and electrons in crystal lattices intrinsically, can be also utilized for sunlight-driven catalysis. The spatial charge separation in photoelectrodes, as well as on oxynitride particles, is likely to be necessary for efficient, stable photoreactions. In particulate photoelectrodes, the electron transfer from

oxynitride particles to a conductive substrate is significantly resistive due to the loose adhesion between them. The bottom-up fabrication to directly grow oxynitride crystals on the conductive substrate can be a solution to obtain a fast electron pathway comparable to the hole transfer rate to surfaces of oxynitrides. Therefore, both the novel synthesis of less-defective oxynitrides to reduce the recombination of photogenerated charges and the surface design of the oxynitrides to make spatially selective separation and transfer of the charges must be challenges to achieving efficient, stable sunlight-driven artificial synthesis using perovskite and layered perovskite oxynitrides.

The overall water splitting of perovskite and layered perovskite oxynitrides by one-step photoexcitation can be the most ideal way to facilitate the low-cost production of H<sub>2</sub> gas on a large scale. The overall water splitting of a ATaO<sub>2</sub>N (A = Sr, Ba) particle has been demonstrated; however its activity is still limited. The separation of both HER and OER sites at the oxynitride surface is likely to be necessary to drive water splitting, while HER sites with a cocatalyst were distinguished from the surface of oxides such as SrTiO<sub>3</sub>. The selective deposition of the cocatalyst and crystal facet engineering of the oxynitrides are challenging for efficient overall water splitting. In a PEC system, the anodic photoresponse of perovskite and layered perovskite oxynitrides should be below 0 V<sub>RHE</sub> based on their flat band potentials (which are negative). However, the actual photocurrent onset is limited to the range of 0.5 to 0.6 V<sub>RHE</sub>. Unassisted solar water splitting *via* PEC cells comprising perovskite and layered perovskite oxynitrides combined with other cathode materials has rarely been reported. Thus, efficient photoanodes must be able to generate significant photocurrent density at a moderate potential (0.4 to 0.6 V<sub>RHE</sub>) based on the overlap with the photocathode during overall water splitting. It is necessary to apply various approaches to improve their water-splitting activity by, for instance, optimizing their optical and physical properties. Moreover, a better understanding of the effect of pH (photoanodes are more active at higher pH values while photocathodes work well at lower pH values) must also be achieved to obtain a high rate of H<sub>2</sub> production. Therefore, these challenges are directly related to the photoactivity and long-term stability of these materials for efficient artificial photosynthesis.

## Conflicts of interest

The authors have no conflicts of interest relevant to this study to disclose.

## Acknowledgements

This research was financially supported by the Basic Science Research Program (no. RS-2023-00243439) and Regional Innovation Strategy (RIS) (no. 2021RIS-002) through the National Research Foundation of Korea (NRF) funded by the Ministry of Education (MOE). This study was also supported by the NRF grant funded by the Korean government (MSIT) (no. 2021M3I3A1084818).



## References

- G. Zhang, G. Liu, L. Wang and J. T. Irvine, Inorganic perovskite photocatalysts for solar energy utilization, *Chem. Soc. Rev.*, 2016, **45**, 5951–5984.
- T. Hisatomi, J. Kubota and K. Domen, Recent advances in semiconductors for photocatalytic and photoelectrochemical water splitting, *Chem. Soc. Rev.*, 2014, **43**, 7520–7535.
- J. Seo, H. Nishiyama, T. Yamada and K. Domen, Visible-Light-Responsive Photoanodes for Highly Active, Stable Water Oxidation, *Angew. Chem., Int. Ed.*, 2018, **57**, 8396–8415.
- H. Fujito, H. Kunioku, D. Kato, H. Suzuki, M. Higashi, H. Kageyama and R. Abe, Layered Perovskite Oxochloride  $\text{Bi}_4\text{NbO}_8\text{Cl}$ : A Stable Visible Light Responsive Photocatalyst for Water Splitting, *J. Am. Chem. Soc.*, 2016, **138**, 2082–2085.
- A. Nakada, M. Higashi, T. Kimura, H. Suzuki, D. Kato, H. Okajima, T. Yamamoto, A. Saeki, H. Kageyama and R. Abe, Band Engineering of Double-Layered Sillén–Aurivillius Perovskite Oxochlorides for Visible-Light-Driven Water Splitting, *Chem. Mater.*, 2019, **31**, 3419–3429.
- M. Hojamberdiev, M. F. Bekheet, E. Zahedi, H. Wagata, Y. Kamei, K. Yubuta, A. Gurlo, N. Matsushita, K. Domen and K. Teshima, New Dion–Jacobson Phase Three-Layer Perovskite  $\text{CsBa}_2\text{Ta}_3\text{O}_{10}$  and Its Conversion to Nitrided  $\text{Ba}_2\text{Ta}_3\text{O}_{10}$  Nanosheets *via* a Nitridation–Protonation–Intercalation–Exfoliation Route for Water Splitting, *Cryst. Growth Des.*, 2016, **16**, 2302–2308.
- Y. Suemoto, Y. Masubuchi, Y. Nagamine, A. Matsutani, T. Shibahara, K. Yamazaki and S. Kikkawa, Intergrowth between the Oxynitride Perovskite  $\text{SrTaO}_2\text{N}$  and the Ruddlesden–Popper Phase  $\text{Sr}_2\text{TaO}_3\text{N}$ , *Inorg. Chem.*, 2018, **57**, 9086–9095.
- G. Gou, M. Zhao, J. Shi, J. K. Harada and J. M. Rondinelli, Anion Ordered and Ferroelectric Ruddlesden–Popper Oxynitride  $\text{Ca}_3\text{Nb}_2\text{N}_2\text{O}_5$  for Visible-Light-Active Photocatalysis, *Chem. Mater.*, 2020, **32**, 2815–2823.
- Y. Tang, K. Kato, T. Oshima, H. Mogi, A. Miyoshi, K. Fujii, K. I. Yanagisawa, K. Kimoto, A. Yamakata, M. Yashima and K. Maeda, Synthesis of Three-Layer Perovskite Oxynitride  $\text{K}_2\text{Ca}_2\text{Ta}_3\text{O}_9\text{N}\cdot 2\text{H}_2\text{O}$  and Photocatalytic Activity for  $\text{H}_2$  Evolution under Visible Light, *Inorg. Chem.*, 2020, **59**, 11122–11128.
- Y. Shiroma, H. Mogi, T. Mashiko, S. Yasuda, S. Nishioka, T. Yokoi, S. Ida, K. Kimoto and K. Maeda, Interlayer modification and single-layer exfoliation of the Ruddlesden–Popper perovskite oxynitride  $\text{K}_2\text{LaTa}_2\text{O}_6\text{N}$  to improve photocatalytic  $\text{H}_2$  evolution activity, *J. Mater. Chem. A*, 2023, **11**, 9485–9492.
- Y. Ham, T. Hisatomi, Y. Goto, Y. Moriya, Y. Sakata, A. Yamakata, J. Kubota and K. Domen, Flux-mediated doping of  $\text{SrTiO}_3$  photocatalysts for efficient overall water splitting, *J. Mater. Chem. A*, 2016, **4**, 3027–3033.
- T. Takata, J. Jiang, Y. Sakata, M. Nakabayashi, N. Shibata, V. Nandal, K. Seki, T. Hisatomi and K. Domen, Photocatalytic water splitting with a quantum efficiency of almost unity, *Nature*, 2020, **581**, 411–414.
- Y. Miseki, H. Kato and A. Kudo, Water Splitting into  $\text{H}_2$  and  $\text{O}_2$  over  $\text{Ba}_5\text{Nb}_4\text{O}_{15}$  Photocatalysts with Layered Perovskite Structure Prepared by Polymerizable Complex Method, *Chem. Lett.*, 2006, **35**, 1052–1053.
- W.-J. Chun, A. Ishikawa, H. Fujisawa, T. Takata, J. N. Kondo, M. Hara, M. Kawai, Y. Matsumoto and K. Domen, Conduction and Valence Band Positions of  $\text{Ta}_2\text{O}_5$ ,  $\text{TaON}$ , and  $\text{Ta}_3\text{N}_5$  by UPS and Electrochemical Methods, *J. Phys. Chem. B*, 2003, **107**, 1798–1803.
- S. Ramaraj and J. Seo, Intensive-visible-light-responsive  $\text{ANbO}_2\text{N}$  ( $\text{A} = \text{Sr}, \text{Ba}$ ) synthesized from layered perovskite  $\text{A}_5\text{Nb}_4\text{O}_{15}$  for enhanced photoelectrochemical water splitting, *J. Energy Chem.*, 2022, **68**, 529–537.
- F. Zhang, A. Yamakata, K. Maeda, Y. Moriya, T. Takata, J. Kubota, K. Teshima, S. Oishi and K. Domen, Cobalt-modified porous single-crystalline  $\text{LaTiO}_2\text{N}$  for highly efficient water oxidation under visible light, *J. Am. Chem. Soc.*, 2012, **134**, 8348–8351.
- S. Akiyama, M. Nakabayashi, N. Shibata, T. Minegishi, Y. Asakura, M. Abdulla-Al-Mamun, T. Hisatomi, H. Nishiyama, M. Katayama, T. Yamada and K. Domen, Highly Efficient Water Oxidation Photoanode Made of Surface Modified  $\text{LaTiO}_2\text{N}$  Particles, *Small*, 2016, **12**, 5468–5476.
- J. Seo, T. Hisatomi, M. Nakabayashi, N. Shibata, T. Minegishi, M. Katayama and K. Domen, Efficient Solar-Driven Water Oxidation over Perovskite-Type  $\text{BaNbO}_2\text{N}$  Photoanodes Absorbing Visible Light up to 740 nm, *Adv. Energy Mater.*, 2018, **8**, 1800094.
- J. Seo, M. Nakabayashi, T. Hisatomi, N. Shibata, T. Minegishi and K. Domen, Solar-Driven Water Splitting over a  $\text{BaTaO}_2\text{N}$  Photoanode Enhanced by Annealing in Argon, *ACS Appl. Energy Mater.*, 2019, **2**, 5777–5784.
- K. Maeda and K. Domen, New Non-Oxide Photocatalysts Designed for Overall Water Splitting under Visible Light, *J. Phys. Chem. C*, 2007, **111**, 7851–7861.
- H. W. Eng, P. W. Barnes, B. M. Auer and P. M. Woodward, Investigations of the electronic structure of  $d_0$  transition metal oxides belonging to the perovskite family, *J. Solid State Chem.*, 2003, **175**, 94–109.
- S. Balaz, S. H. Porter, P. M. Woodward and L. J. Brillson, Electronic Structure of Tantalum Oxynitride Perovskite Photocatalysts, *Chem. Mater.*, 2013, **25**, 3337–3343.
- T. W. Kim and K.-S. Choi, Nanoporous  $\text{BiVO}_4$  Photoanodes with Dual-Layer Oxygen Evolution Catalysts for Solar Water Splitting, *Science*, 2014, **343**, 990–994.
- Y. Kuang, Q. Jia, G. Ma, T. Hisatomi, T. Minegishi, H. Nishiyama, M. Nakabayashi, N. Shibata, T. Yamada, A. Kudo and K. Domen, Ultrastable low-bias water splitting photoanodes *via* photocorrosion inhibition and *in situ* catalyst regeneration, *Nat. Energy*, 2017, **2**, 16191.
- P. Sharma, J. W. Jang and J. S. Lee, Key Strategies to Advance the Photoelectrochemical Water Splitting Performance of  $\alpha\text{-Fe}_2\text{O}_3$  Photoanode, *ChemCatChem*, 2018, **11**, 157–179.
- T. Oshima, T. Ichihara, K. S. Qin, K. Muraoka, J. J. M. Vequizo, K. Hibino, R. Kuriki, S. Yamashita, K. Hongo, T. Uchiyama, K. Fujii, D. Lu, R. Maezono, A. Yamakata, H. Kato, K. Kimoto, M. Yashima, Y. Uchimoto, M. Kakihana, O. Ishitani,

- H. Kageyama and K. Maeda, Undoped Layered Perovskite Oxynitride  $\text{Li}_2\text{LaTa}_2\text{O}_6\text{N}$  for Photocatalytic  $\text{CO}_2$  Reduction with Visible Light, *Angew. Chem., Int. Ed.*, 2018, **57**, 8154–8158.
- 27 Q. Wang and K. Domen, Particulate Photocatalysts for Light-Driven Water Splitting: Mechanisms, Challenges, and Design Strategies, *Chem. Rev.*, 2020, **120**, 919–985.
- 28 X. M. C. Ta, R. Daiyan, T. K. A. Nguyen, R. Amal, T. Tran-Phu and A. Tricoli, Alternatives to Water Photooxidation for Photoelectrochemical Solar Energy Conversion and Green  $\text{H}_2$  Production, *Adv. Energy Mater.*, 2022, **12**, 2201358.
- 29 V.-H. Trinh and J. Seo, Porous Cuboidal  $\text{SrNbO}_2\text{N}$  Crystals Grown on a Nb Substrate as an Active Photoanode for Neutral Seawater Splitting under Sunlight, *ACS Sustainable Chem. Eng.*, 2023, **11**, 1655–1665.
- 30 R. Shi, G. I. N. Waterhouse and T. Zhang, Recent Progress in Photocatalytic  $\text{CO}_2$  Reduction Over Perovskite Oxides, *Sol. RRL*, 2017, **1**, 1700126.
- 31 K. Maeda and T. E. Mallouk, Two-Dimensional Metal Oxide Nanosheets as Building Blocks for Artificial Photosynthetic Assemblies, *Bull. Chem. Soc. Jpn.*, 2019, **92**, 38–54.
- 32 A. Murphy, P. Barnes, L. Randeniya, I. Plumb, I. Grey, M. Horne and J. Glasscock, Efficiency of solar water splitting using semiconductor electrodes, *Int. J. Hydrogen Energy*, 2006, **31**, 1999–2017.
- 33 A. G. Tamirat, J. Rick, A. A. Dubale, W.-N. Su and B.-J. Hwang, Using hematite for photoelectrochemical water splitting: a review of current progress and challenges, *Nanoscale Horiz.*, 2016, **1**, 243–267.
- 34 H. Nishiyama, T. Yamada, M. Nakabayashi, Y. Maehara, M. Yamaguchi, Y. Kuromiya, Y. Nagatsuma, H. Tokudome, S. Akiyama, T. Watanabe, R. Narushima, S. Okunaka, N. Shibata, T. Takata, T. Hisatomi and K. Domen, Photocatalytic solar hydrogen production from water on a 100-m<sup>2</sup> scale, *Nature*, 2021, **598**, 304–307.
- 35 H. Li, J. Xiao, J. J. M. Vequizo, T. Hisatomi, M. Nakabayashi, Z. Wang, N. Shibata, A. Yamakata, T. Takata and K. Domen, One-Step Excitation Overall Water Splitting over a Modified Mg-Doped  $\text{BaTaO}_2\text{N}$  Photocatalyst, *ACS Catal.*, 2022, **12**, 10179–10185.
- 36 K. Chen, J. Xiao, J. J. M. Vequizo, T. Hisatomi, Y. Ma, M. Nakabayashi, T. Takata, A. Yamakata, N. Shibata and K. Domen, Overall Water Splitting by a  $\text{SrTaO}_2\text{N}$ -Based Photocatalyst Decorated with an Ir-Promoted Ru-Based Cocatalyst, *J. Am. Chem. Soc.*, 2023, **145**, 3839–3843.
- 37 X. Wang, K. Maeda, A. Thomas, K. Takanabe, G. Xin, J. M. Carlsson, K. Domen and M. Antonietti, A metal-free polymeric photocatalyst for hydrogen production from water under visible light, *Nat. Mater.*, 2009, **8**, 76–80.
- 38 K. Maeda, K. Teramura, D. Lu, T. Takata, N. Saito, Y. Inoue and K. Domen, Photocatalyst releasing hydrogen from water, *Nature*, 2006, **440**, 295.
- 39 Z. Wang, Y. Inoue, T. Hisatomi, R. Ishikawa, Q. Wang, T. Takata, S. Chen, N. Shibata, Y. Ikuhara and K. Domen, Overall water splitting by  $\text{Ta}_3\text{N}_5$  nanorod single crystals grown on the edges of  $\text{KTaO}_3$  particles, *Nat. Catal.*, 2018, **1**, 756–763.
- 40 Q. Wang, M. Nakabayashi, T. Hisatomi, S. Sun, S. Akiyama, Z. Wang, Z. Pan, X. Xiao, T. Watanabe, T. Yamada, N. Shibata, T. Takata and K. Domen, Oxysulfide photocatalyst for visible-light-driven overall water splitting, *Nat. Mater.*, 2019, **18**, 827–832.
- 41 C. Pan, T. Takata, M. Nakabayashi, T. Matsumoto, N. Shibata, Y. Ikuhara and K. Domen, A complex perovskite-type oxynitride: the first photocatalyst for water splitting operable at up to 600 nm, *Angew. Chem., Int. Ed.*, 2015, **54**, 2955–2959.
- 42 J. Seo, D. Ishizuka, T. Hisatomi, T. Takata and K. Domen, Effect of  $\text{Mg}^{2+}$  substitution on the photocatalytic water splitting activity of  $\text{LaMg}_x\text{Nb}_{1-x}\text{O}_{1+3x}\text{N}_{2-3x}$ , *J. Mater. Chem. A*, 2021, **9**, 8655–8662.
- 43 K. Maeda, K. Teramura, D. Lu, N. Saito, Y. Inoue and K. Domen, Roles of  $\text{Rh/Cr}_2\text{O}_3$  (core/shell) nanoparticles photo-deposited on visible light responsive  $(\text{Ga}_{1-x}\text{Zn}_x)(\text{N}_{1-x}\text{O}_x)$  solid solutions in photocatalytic overall water splitting, *J. Phys. Chem. C*, 2007, **111**, 7554–7560.
- 44 M. Yoshida, K. Takanabe, K. Maeda, A. Ishikawa, J. Kubota, Y. Sakata, Y. Ikezawa and K. Domen, Role and Function of Noble-Metal/Cr-Layer Core/Shell Structure Cocatalysts for Photocatalytic Overall Water Splitting Studied by Model Electrodes, *J. Phys. Chem. C*, 2009, **113**, 10151–10157.
- 45 H. Kato, K. Asakura and A. Kudo, Highly Efficient Water Splitting into  $\text{H}_2$  and  $\text{O}_2$  over Lanthanum-Doped  $\text{NaTaO}_3$  Photocatalysts with High Crystallinity and Surface Nanostructure, *J. Am. Chem. Soc.*, 2003, **125**, 3082–3089.
- 46 C. Pan, T. Takata, K. Kumamoto, S. S. Khine Ma, K. Ueda, T. Minegishi, M. Nakabayashi, T. Matsumoto, N. Shibata, Y. Ikuhara and K. Domen, Band engineering of perovskite-type transition metal oxynitrides for photocatalytic overall water splitting, *J. Mater. Chem. A*, 2016, **4**, 4544–4552.
- 47 J. H. Kim, D. Hansora, P. Sharma, J. W. Jang and J. S. Lee, Toward practical solar hydrogen production – an artificial photosynthetic leaf-to-farm challenge, *Chem. Soc. Rev.*, 2019, **48**, 1908–1971.
- 48 Y. Zhang, H. Lv, Z. Zhang, L. Wang, X. Wu and H. Xu, Stable Unbiased Photo-Electrochemical Overall Water Splitting Exceeding 3% Efficiency via Covalent Triazine Framework/Metal Oxide Hybrid Photoelectrodes, *Adv. Mater.*, 2021, **33**, e2008264.
- 49 S. Ye, W. Shi, Y. Liu, D. Li, H. Yin, H. Chi, Y. Luo, N. Ta, F. Fan, X. Wang and C. Li, Unassisted Photoelectrochemical Cell with Multimediator Modulation for Solar Water Splitting Exceeding 4% Solar-to-Hydrogen Efficiency, *J. Am. Chem. Soc.*, 2021, **143**, 12499–12508.
- 50 R. Rhee, T. G. Kim, G. Y. Jang, G. Bae, J. H. Lee, S. Lee, S. Kim, S. Jeon and J. H. Park, Unassisted overall water splitting with a solar-to-hydrogen efficiency of over 10% by coupled lead halide perovskite photoelectrodes, *Carbon Energy*, 2022, **5**, 1–10.
- 51 T. Higashi, Y. Shinohara, A. Ohnishi, J. Liu, K. Ueda, S. Okamura, T. Hisatomi, M. Katayama, H. Nishiyama, T. Yamada, T. Minegishi and K. Domen, Sunlight-Driven Overall Water Splitting by the Combination of

- Surface-Modified  $\text{La}_5\text{Ti}_2\text{Cu}_{0.9}\text{Ag}_{0.1}\text{S}_5\text{O}_7$  and  $\text{BaTaO}_2\text{N}$  Photoelectrodes, *ChemPhotoChem*, 2016, **1**, 1–7.
- 52 M. Cao, H. Li, K. Liu, J. Hu, H. Pan, J. Fu and M. Liu, Vertical  $\text{SrNbO}_2\text{N}$  Nanorod Arrays for Solar-Driven Photoelectrochemical Water Splitting, *Sol. RRL*, 2020, **5**, 2000448.
- 53 J. Seo, M. Nakabayashi, T. Hisatomi, N. Shibata, T. Minegishi, M. Katayama and K. Domen, The effects of annealing barium niobium oxynitride in argon on photoelectrochemical water oxidation activity, *J. Mater. Chem. A*, 2019, **7**, 493–502.
- 54 M. Matsukawa, R. Ishikawa, T. Hisatomi, Y. Moriya, N. Shibata, J. Kubota, Y. Ikuhara and K. Domen, Enhancing photocatalytic activity of  $\text{LaTiO}_2\text{N}$  by removal of surface reconstruction layer, *Nano Lett.*, 2014, **14**, 1038–1041.
- 55 C. R. Lhermitte and K. Sivula, Alternative Oxidation Reactions for Solar-Driven Fuel Production, *ACS Catal.*, 2019, **9**, 2007–2017.
- 56 J. C. Hill and K.-S. Choi, Effect of Electrolytes on the Selectivity and Stability of n-type  $\text{WO}_3$  Photoelectrodes for Use in Solar Water Oxidation, *J. Phys. Chem. C*, 2012, **116**, 7612–7620.
- 57 F. Dionigi, T. Reier, Z. Pawolek, M. Gliech and P. Strasser, Design Criteria, Operating Conditions, and Nickel-Iron Hydroxide Catalyst Materials for Selective Seawater Electrolysis, *ChemSusChem*, 2016, **9**, 962–972.
- 58 M. Jadwiszczak, K. Jakubow-Piotrowska, P. Kedzierzawski, K. Bienkowski and J. Augustynski, Highly Efficient Sunlight-Driven Seawater Splitting in a Photoelectrochemical Cell with Chlorine Evolved at Nanostructured  $\text{WO}_3$  Photoanode and Hydrogen Stored as Hydride within Metallic Cathode, *Adv. Energy Mater.*, 2019, **10**, 1903213.
- 59 S. Iguchi, Y. Miseki and K. Sayama, Efficient hypochlorous acid ( $\text{HClO}$ ) production *via* photo electrochemical solar energy conversion using a  $\text{BiVO}_4$ -based photoanode, *Sustainable Energy Fuels*, 2018, **2**, 155–162.
- 60 R.-T. Gao, X. Guo, S. Liu, X. Zhang, X. Liu, Y. Su and L. Wang, Ultrastable and high-performance seawater-based photoelectrolysis system for solar hydrogen generation, *Appl. Catal., B*, 2022, **304**, 120883.
- 61 M. Higashi, K. Domen and R. Abe, Fabrication of an efficient  $\text{BaTaO}_2\text{N}$  photoanode harvesting a wide range of visible light for water splitting, *J. Am. Chem. Soc.*, 2013, **135**, 10238–10241.
- 62 K. Ueda, T. Minegishi, J. Clune, M. Nakabayashi, T. Hisatomi, H. Nishiyama, M. Katayama, N. Shibata, J. Kubota, T. Yamada and K. Domen, Photoelectrochemical oxidation of water using  $\text{BaTaO}_2\text{N}$  photoanodes prepared by particle transfer method, *J. Am. Chem. Soc.*, 2015, **137**, 2227–2230.
- 63 K. Takanabe, Photocatalytic Water Splitting: Quantitative Approaches toward Photocatalyst by Design, *ACS Catal.*, 2017, **7**, 8006–8022.
- 64 J. Liu, Y. Zou, B. Jin, K. Zhang and J. H. Park, Hydrogen Peroxide Production from Solar Water Oxidation, *ACS Energy Lett.*, 2019, **4**, 3018–3027.
- 65 H. Hou, X. Zeng and X. Zhang, Production of Hydrogen Peroxide by Photocatalytic Processes, *Angew. Chem., Int. Ed.*, 2020, **59**, 17356–17376.
- 66 K. Mase, M. Yoneda, Y. Yamada and S. Fukuzumi, Seawater usable for production and consumption of hydrogen peroxide as a solar fuel, *Nat. Commun.*, 2016, **7**, 11470.
- 67 Y. Miyase, S. Takasugi, S. Iguchi, Y. Miseki, T. Gunji, K. Sasaki, E. Fujita and K. Sayama, Modification of  $\text{BiVO}_4/\text{WO}_3$  composite photoelectrodes with  $\text{Al}_2\text{O}_3$  *via* chemical vapor deposition for highly efficient oxidative  $\text{H}_2\text{O}_2$  production from  $\text{H}_2\text{O}$ , *Sustainable Energy Fuels*, 2018, **2**, 1621–1629.
- 68 Y. Miseki and K. Sayama, Photocatalytic Water Splitting for Solar Hydrogen Production Using the Carbonate Effect and the Z-Scheme Reaction, *Adv. Energy Mater.*, 2018, **9**, 1801294.
- 69 J. H. Baek, T. M. Gill, H. Abroshan, S. Park, X. Shi, J. Nørskov, H. S. Jung, S. Siahrostami and X. Zheng, Selective and Efficient Gd-Doped  $\text{BiVO}_4$  Photoanode for Two-Electron Water Oxidation to  $\text{H}_2\text{O}_2$ , *ACS Energy Lett.*, 2019, **4**, 720–728.
- 70 R. Saito, Y. Miseki and K. Sayama, Highly efficient photoelectrochemical water splitting using a thin film photoanode of  $\text{BiVO}_4/\text{SnO}_2/\text{WO}_3$  multi-composite in a carbonate electrolyte, *Chem. Commun.*, 2012, **48**, 3833.
- 71 S. N. Habisreutinger, L. Schmidt-Mende and J. K. Stolarczyk, Photocatalytic reduction of  $\text{CO}_2$  on  $\text{TiO}_2$  and other semiconductors, *Angew. Chem., Int. Ed.*, 2013, **52**, 7372–7408.
- 72 J. Ran, M. Jaroniec and S. Z. Qiao, Cocatalysts in Semiconductor-based Photocatalytic  $\text{CO}_2$  Reduction: Achievements, Challenges, and Opportunities, *Adv. Mater.*, 2018, **30**, 1704649.
- 73 E. Kalamaras, M. M. Maroto-Valer, M. Shao, J. Xuan and H. Wang, Solar carbon fuel *via* photoelectrochemistry, *Catal. Today*, 2018, **317**, 56–75.
- 74 H. Kumagai, Y. Tamaki and O. Ishitani, Photocatalytic Systems for  $\text{CO}_2$  Reduction: Metal-Complex Photocatalysts and Their Hybrids with Photofunctional Solid Materials, *Acc. Chem. Res.*, 2022, **55**, 978–990.
- 75 H. Kumagai, G. Sahara, K. Maeda, M. Higashi, R. Abe and O. Ishitani, Hybrid photocathode consisting of a  $\text{CuGaO}_2$  p-type semiconductor and a  $\text{Ru(II)-Re(I)}$  supramolecular photocatalyst: non-biased visible-light-driven  $\text{CO}_2$  reduction with water oxidation, *Chem. Sci.*, 2017, **8**, 4242–4249.
- 76 F. Yoshitomi, K. Sekizawa, K. Maeda and O. Ishitani, Selective Formic Acid Production *via*  $\text{CO}_2$  Reduction with Visible Light Using a Hybrid of a Perovskite Tantalum Oxynitride and a Binuclear Ruthenium(II) Complex, *ACS Appl. Mater. Interfaces*, 2015, **7**, 13092–13097.
- 77 T. Oshima, T. Ichibha, K. Oqmhula, K. Hibino, H. Mogi, S. Yamashita, K. Fujii, Y. Miseki, K. Hongo, D. Lu, R. Maezono, K. Sayama, M. Yashima, K. Kimoto, H. Kato, M. Kakihana, H. Kageyama and K. Maeda, Two-Dimensional Perovskite Oxynitride  $\text{K}_2\text{LaTa}_2\text{O}_6\text{N}$  with an  $\text{H}^{(+)}/\text{K}^{(+)}$  Exchangeability in Aqueous Solution Forming a Stable Photocatalyst for Visible-Light  $\text{H}_2$  Evolution, *Angew. Chem., Int. Ed.*, 2020, **59**, 9736–9743.
- 78 H. Zhou, Y. Luo, J. Xu, L. Deng, Z. Wang and H. He, Bicomponent Cocatalyst Decoration on Flux-assisted  $\text{CaTaO}_2\text{N}$  Single Crystals for Photocatalytic  $\text{CO}_2$  Reduction under Visible Light, *Chem. – Eur. J.*, 2022, **28**, e202202044.



- 79 P. Lin, L. Xiao, Y. Lu, Z. Zhang, X. Wang and W. Su, Anchoring 0D CeO<sub>2</sub> Nanoparticles on 2D LaTiO<sub>2</sub>N Nanosheets for Efficient Visible-Light-Driven Photocatalytic CO<sub>2</sub> Reduction, *ChemCatChem*, 2022, **14**, e202201041.
- 80 L. Lin, P. Lin, J. Song, Z. Zhang, X. Wang and W. Su, Boosting the photocatalytic activity and stability of Cu<sub>2</sub>O for CO<sub>2</sub> conversion by LaTiO<sub>2</sub>N, *J. Colloid Interface Sci.*, 2023, **630**, 352–362.
- 81 H. Urabe, T. Hisatomi, T. Minegishi, J. Kubota and K. Domen, Photoelectrochemical properties of SrNbO<sub>2</sub>N photoanodes for water oxidation fabricated by the particle transfer method, *Faraday Discuss.*, 2014, **176**, 213–223.
- 82 J. Xu, C. Pan, T. Takata and K. Domen, Photocatalytic overall water splitting on the perovskite-type transition metal oxynitride CaTaO<sub>2</sub>N under visible light irradiation, *Chem. Commun.*, 2015, **51**, 7191–7194.
- 83 S. Wei and X. Xu, Boosting photocatalytic water oxidation reactions over strontium tantalum oxynitride by structural laminations, *Appl. Catal., B*, 2018, **228**, 10–18.
- 84 S. Nishimae, Y. Mishima, H. Nishiyama, Y. Sasaki, M. Nakabayashi, Y. Inoue, M. Katayama and K. Domen, Fabrication of BaTaO<sub>2</sub>N Thin Films by Interfacial Reactions of BaCO<sub>3</sub>/Ta<sub>3</sub>N<sub>5</sub> Layers on a Ta Substrate and Resulting High Photoanode Efficiencies During Water Splitting, *Sol. RRL*, 2020, **4**, 1900542.
- 85 Y. Xiang, B. Zhang, J. Liu, S. Chen, T. Hisatomi, K. Domen and G. Ma, A one-step synthesis of a Ta<sub>3</sub>N<sub>5</sub> nanorod photoanode from Ta plates and NH<sub>4</sub>Cl powder for photoelectrochemical water oxidation, *Chem. Commun.*, 2020, **56**, 11843–11846.
- 86 B. Siritanaratkul, K. Maeda, T. Hisatomi and K. Domen, Synthesis and photocatalytic activity of perovskite niobium oxynitrides with wide visible-light absorption bands, *ChemSusChem*, 2011, **4**, 74–78.
- 87 K. Maeda and K. Domen, Water oxidation using a particulate BaZrO<sub>3</sub>-BaTaO<sub>2</sub>N solid-solution photocatalyst that operates under a wide range of visible light, *Angew. Chem., Int. Ed.*, 2012, **51**, 9865–9869.
- 88 T. T. T. Tran, S. Kim and J. Seo, Size dependence of perovskite-type BaNbO<sub>2</sub>N particles on sunlight-driven photoelectrochemical water splitting, *J. Catal.*, 2022, **406**, 157–164.
- 89 T. Oshima, T. Ichibha, K. Oqmhula, K. Hibino, H. Mogi, S. Yamashita, K. Fujii, Y. Miseki, K. Hongo, D. Lu, R. Maezono, K. Sayama, M. Yashima, K. Kimoto, H. Kato, M. Kakihana, H. Kageyama and K. Maeda, Two-Dimensional Perovskite Oxynitride K<sub>2</sub>LaTa<sub>2</sub>O<sub>6</sub>N with an H<sup>+</sup>/K<sup>+</sup> Exchangeability in Aqueous Solution Forming a Stable Photocatalyst for Visible-Light H<sub>2</sub> Evolution, *Angew. Chem., Int. Ed.*, 2020, **59**, 9736–9743.
- 90 J. Seo, Y. Moriya, M. Kodera, T. Hisatomi, T. Minegishi, M. Katayama and K. Domen, Photoelectrochemical Water Splitting on Particulate ANbO<sub>2</sub>N (A = Ba, Sr) Photoanodes Prepared from Perovskite-Type ANbO<sub>3</sub>, *Chem. Mater.*, 2016, **28**, 6869–6876.
- 91 T. Hisatomi, C. Katayama, Y. Moriya, T. Minegishi, M. Katayama, H. Nishiyama, T. Yamada and K. Domen, Photocatalytic oxygen evolution using BaNbO<sub>2</sub>N modified with cobalt oxide under photoexcitation up to 740 nm, *Energy Environ. Sci.*, 2013, **6**, 3595.
- 92 M. Hojamberdiev, K. Yubuta, J. J. M. Vequizo, A. Yamakata, S. Oishi, K. Domen and K. Teshima, NH<sub>3</sub>-Assisted Flux Growth of Cube-like BaTaO<sub>2</sub>N Submicron Crystals in a Completely Ionized Nonaqueous High-Temperature Solution and Their Water Splitting Activity, *Cryst. Growth Des.*, 2015, **15**, 4663–4671.
- 93 M. Kodera, H. Urabe, M. Katayama, T. Hisatomi, T. Minegishi and K. Domen, Effects of flux synthesis on SrNbO<sub>2</sub>N particles for photoelectrochemical water splitting, *J. Mater. Chem. A*, 2016, **4**, 7658–7664.
- 94 J. Seo, Size Control of LaNbON<sub>2</sub> Particles for Enhanced Photocatalytic Water Oxidation Under Visible Light Irradiation, *Bull. Korean Chem. Soc.*, 2021, **42**, 571–576.
- 95 J. Seo, S. Jeong and S. Kim, Visible-Light-Driven Water Splitting over Particulate LaNbON<sub>2</sub> Prepared from La-Rich Lanthanum Niobium Oxides, *ACS Appl. Energy Mater.*, 2021, **4**, 3141–3150.
- 96 T. Hisatomi, C. Katayama, K. Teramura, T. Takata, Y. Moriya, T. Minegishi, M. Katayama, H. Nishiyama, T. Yamada and K. Domen, The effects of preparation conditions for a BaNbO<sub>2</sub>N photocatalyst on its physical properties, *ChemSusChem*, 2014, **7**, 2016–2021.
- 97 X. Xu, C. Random, P. Efstathiou and J. T. Irvine, A red metallic oxide photocatalyst, *Nat. Mater.*, 2012, **11**, 595–598.
- 98 D. Lu, G. Hitoki, E. Katou, J. N. Kondo, M. Hara and K. Domen, Porous Single-Crystalline TaON and Ta<sub>3</sub>N<sub>5</sub> Particles, *Chem. Mater.*, 2004, **16**, 1603–1605.
- 99 S. Jadhav, S. Hasegawa, T. Hisatomi, Z. Wang, J. Seo, T. Higashi, M. Katayama, T. Minegishi, T. Takata, J. M. Peralta-Hernández, O. Serrano Torres and K. Domen, Efficient photocatalytic oxygen evolution using BaTaO<sub>2</sub>N obtained from nitridation of perovskite-type oxide, *J. Mater. Chem. A*, 2020, **8**, 1127–1130.
- 100 D. E. Bugaris and H. C. zur Loye, Materials discovery by flux crystal growth: quaternary and higher order oxides, *Angew. Chem., Int. Ed.*, 2012, **51**, 3780–3811.
- 101 T. Yamada, Y. Murata, H. Wagata, K. Yubuta and K. Teshima, Facile Morphological Modification of Ba<sub>5</sub>Nb<sub>4</sub>O<sub>15</sub> Crystals Using Chloride Flux and *in Situ* Growth Investigation, *Cryst. Growth Des.*, 2016, **16**, 3954–3960.
- 102 L. Zhang, Y. Song, J. Feng, T. Fang, Y. Zhong, Z. Li and Z. Zou, Photoelectrochemical water oxidation of LaTaON<sub>2</sub> under visible-light irradiation, *Int. J. Hydrogen Energy*, 2014, **39**, 7697–7704.
- 103 Y. Luo, Z. Wang, S. Suzuki, K. Yubuta, N. Kariya, T. Hisatomi, K. Domen and K. Teshima, Fabrication of Single-Crystalline BaTaO<sub>2</sub>N from Chloride Fluxes for Photocatalytic H<sub>2</sub> Evolution under Visible Light, *Cryst. Growth Des.*, 2019, **20**, 255–261.
- 104 T. Minegishi, N. Nishimura, J. Kubota and K. Domen, Photoelectrochemical properties of LaTiO<sub>2</sub>N electrodes prepared by particle transfer for sunlight-driven water splitting, *Chem. Sci.*, 2013, **4**, 1120–1124.

- 105 T. T. T. Tran, V.-H. Trinh and J. Seo, Two-dimensional perovskite SrNbO<sub>2</sub>N with Zr doping for accelerating photoelectrochemical water splitting, *J. Mater. Sci. Technol.*, 2023, **142**, 176–184.
- 106 M. V. Kelso, N. K. Mahenderkar, Q. Chen, J. Z. Tubbesing and J. A. Switzer, Spin coating epitaxial films, *Science*, 2019, **364**, 166–169.
- 107 S. G. Ebbinghaus, H.-P. Abicht, R. Dronskowski, T. Müller, A. Reller and A. Weidenkaff, Perovskite-related oxynitrides – Recent developments in synthesis, characterisation and investigations of physical properties, *Prog. Solid State Chem.*, 2009, **37**, 173–205.
- 108 M. D. Tyona, A theoretical study on spin coating technique, *Adv. Mater. Res.*, 2013, **2**, 195–208.
- 109 H. Takeuchi, D. Miyamoto, Y. Masubuchi, M. Higuchi, K. Ishii and T. Uchikoshi, Preparation of thick dense ceramic films of dielectric BaTaO<sub>2</sub>N through electrophoretic deposition, *Ceram. Int.*, 2023, **49**, 21825–21829.
- 110 R. Abe, T. Takata, H. Sugihara and K. Domen, The Use of TiCl<sub>4</sub> Treatment to Enhance the Photocurrent in a TaON Photoelectrode under Visible Light Irradiation, *Chem. Lett.*, 2005, **34**, 1162–1163.
- 111 M. Pichler, W. Si, F. Haydous, H. Téllez, J. Druce, E. Fabbri, M. E. Kazzi, M. Döbeli, S. Ninova, U. Aschauer, A. Wokaun, D. Pergolesi and T. Lippert, LaTiO<sub>x</sub>N<sub>y</sub> Thin Film Model Systems for Photocatalytic Water Splitting: Physicochemical Evolution of the Solid-Liquid Interface and the Role of the Crystallographic Orientation, *Adv. Funct. Mater.*, 2017, **27**, 1605690.
- 112 K. Kawashima, M. Hojamberdiev, O. Mabayoje, B. R. Wygant, K. Yubuta, C. B. Mullins, K. Domen and K. Teshima, NH<sub>3</sub>-assisted chloride flux-coating method for direct fabrication of visible-light-responsive SrNbO<sub>2</sub>N crystal layers, *CrystEngComm*, 2017, **19**, 5532–5541.
- 113 X. Luo, Y. Xiao, B. Zhang, C. Feng, Z. Fan and Y. Li, Direct synthesis of BaTaO<sub>2</sub>N nanoparticle film on a conductive substrate for photoelectrochemical water splitting, *J. Catal.*, 2022, **411**, 109–115.
- 114 X. Xu, W. Wang, Y. Zhang, Y. Chen, H. Huang, T. Fang, Y. Li, Z. Li and Z. Zou, Centimeter-scale perovskite SrTaO<sub>2</sub>N single crystals with enhanced photoelectrochemical performance, *Sci. Bull.*, 2022, **67**, 1458–1466.
- 115 Y.-I. Kim, P. M. Woodward, K. Z. Baba-Kishi and C. W. Tai, Characterization of the Structural, Optical, and Dielectric Properties of Oxynitride Perovskites AMO<sub>2</sub>N (A = Ba, Sr, Ca; M = Ta, Nb), *Chem. Mater.*, 2004, **16**, 1267–1276.
- 116 T. Iwai, A. Nakada, M. Higashi, H. Suzuki, O. Tomita and R. Abe, Controlling the carrier density in niobium oxynitride BaNbO<sub>2</sub>N via cation doping for efficient photoelectrochemical water splitting under visible light, *Sustainable Energy Fuels*, 2021, **5**, 6181–6188.
- 117 M. Hojamberdiev, R. Vargas, Z. C. Kadirova, K. Kato, H. Sena, A. G. Krasnov, A. Yamakata, K. Teshima and M. Lerch, Unfolding the Role of B Site-Selective Doping of Aliovalent Cations on Enhancing Sacrificial Visible Light-Induced Photocatalytic H<sub>2</sub> and O<sub>2</sub> Evolution over BaTaO<sub>2</sub>N, *ACS Catal.*, 2022, **12**, 1403–1414.
- 118 J. Seo, T. Takata, M. Nakabayashi, T. Hisatomi, N. Shibata, T. Minegishi and K. Domen, Mg–Zr Cosubstituted Ta<sub>3</sub>N<sub>5</sub> Photoanode for Lower-Onset-Potential Solar-Driven Photoelectrochemical Water Splitting, *J. Am. Chem. Soc.*, 2015, **137**, 12780–12783.
- 119 Y. Bao, H. Zou, N. Yang, G. Li and F. Zhang, Synthesis of perovskite BaTaO<sub>2</sub>N with low defect by Zn doping for boosted photocatalytic water reduction, *J. Energy Chem.*, 2021, **63**, 358–363.
- 120 Y. Wang, S. Jin, G. Pan, Z. Li, L. Chen, G. Liu and X. Xu, Zr doped mesoporous LaTaON<sub>2</sub> for efficient photocatalytic water splitting, *J. Mater. Chem. A*, 2019, **7**, 5702–5711.
- 121 G. Lin, X. Sun and X. Xu, Mg modified LaTiO<sub>2</sub>N with ameliorated photocarrier separation for solar water splitting, *Appl. Catal., B*, 2023, **324**, 122258.
- 122 X. Sun, Y. Mi, F. Jiao and X. Xu, Activating Layered Perovskite Compound Sr<sub>2</sub>TiO<sub>4</sub> via La/N Codoping for Visible Light Photocatalytic Water Splitting, *ACS Catal.*, 2018, **8**, 3209–3221.
- 123 X. Wang, T. Hisatomi, J. Liang, Z. Wang, Y. Xiang, Y. Zhao, X. Dai, T. Takata and K. Domen, Facet engineering of LaNbON<sub>2</sub> transformed from LaKNaNbO<sub>5</sub> for enhanced photocatalytic O<sub>2</sub> evolution, *J. Mater. Chem. A*, 2020, **8**, 11743–11751.
- 124 M. Shao, A. Peles and K. Shoemaker, Electrocatalysis on platinum nanoparticles: particle size effect on oxygen reduction reaction activity, *Nano Lett.*, 2011, **11**, 3714–3719.
- 125 E. J. Coleman, M. H. Chowdhury and A. C. Co, Insights Into the Oxygen Reduction Reaction Activity of Pt/C and PtCu/C Catalysts, *ACS Catal.*, 2015, **5**, 1245–1253.
- 126 J.-W. Park and J. Seo, Ultrafine TaOx/CB Oxygen Reduction Electrocatalyst Operating in Both Acidic and Alkaline Media, *Catalysts*, 2021, **12**, 35.
- 127 J. Seo, W.-J. Moon, W.-G. Jung and J.-W. Park, A N-doped NbOx nanoparticle electrocatalyst deposited on carbon black for oxygen reduction and evolution reactions in alkaline media, *Mater. Adv.*, 2022, **3**, 5315–5324.
- 128 J. Liu, T. Hisatomi, M. Katayama, T. Minegishi, J. Kubota and K. Domen, Effect of particle size of La<sub>5</sub>Ti<sub>2</sub>CuS<sub>5</sub>O<sub>7</sub> on photoelectrochemical properties in solar hydrogen evolution, *J. Mater. Chem. A*, 2016, **4**, 4848–4854.
- 129 T. Yamada, Y. Murata, S. Suzuki, H. Wagata, S. Oishi and K. Teshima, Template-Assisted Size Control of Polycrystalline BaNbO<sub>2</sub>N Particles and Effects of Their Characteristics on Photocatalytic Water Oxidation Performances, *J. Phys. Chem. C*, 2018, **122**, 8037–8044.
- 130 H. Tsai, W. Nie, J. C. Blancon, C. C. Stoumpos, R. Asadpour, B. Harutyunyan, A. J. Neukirch, R. Verduzco, J. J. Crochet, S. Tretiak, L. Pedesseau, J. Even, M. A. Alam, G. Gupta, J. Lou, P. M. Ajayan, M. J. Bedzyk and M. G. Kanatzidis, High-efficiency two-dimensional Ruddlesden–Popper perovskite solar cells, *Nature*, 2016, **536**, 312–316.
- 131 X. Wang, T. Hisatomi, Z. Wang, J. Song, J. Qu, T. Takata and K. Domen, Core-Shell-Structured LaTaON<sub>2</sub> Transformed from LaKNaTaO<sub>5</sub> Plates for Enhanced Photocatalytic H<sub>2</sub> Evolution, *Angew. Chem., Int. Ed.*, 2019, **58**, 10666–10670.

- 132 C. Lan, Z. Zhou, R. Wei and J. C. Ho, Two-dimensional perovskite materials: From synthesis to energy-related applications, *Mater. Today Energy*, 2019, **11**, 61–82.
- 133 C. Xu, Y. Wang, Q. Guo and X. Wang, Defect engineering of two-dimensional Nb-based oxynitrides for visible-light-driven water splitting to produce H<sub>2</sub> and O<sub>2</sub>, *Nanoscale Adv.*, 2023, **5**, 3260–3266.
- 134 K. Maeda, M. Eguchi, W. J. Youngblood and T. E. Mallouk, Calcium Niobate Nanosheets Prepared by the Polymerized Complex Method as Catalytic Materials for Photochemical Hydrogen Evolution, *Chem. Mater.*, 2009, **21**, 3611–3617.
- 135 Y. L. Cen, J. J. Shi, M. Zhang, M. Wu, J. Du, W. H. Guo and Y. H. Zhu, Optimized band gap and fast interlayer charge transfer in two-dimensional perovskite oxynitride Ba<sub>2</sub>NbO<sub>3</sub>N and Sr<sub>2</sub>NbO<sub>3</sub>/Ba<sub>2</sub>NbO<sub>3</sub>N bonded heterostructure visible-light photocatalysts for overall water splitting, *J. Colloid Interface Sci.*, 2019, **546**, 20–31.
- 136 S. Wang, G. Liu and L. Wang, Crystal Facet Engineering of Photoelectrodes for Photoelectrochemical Water Splitting, *Chem. Rev.*, 2019, **119**, 5192–5247.
- 137 R. Li, F. Zhang, D. Wang, J. Yang, M. Li, J. Zhu, X. Zhou, H. Han and C. Li, Spatial separation of photogenerated electrons and holes among (010) and (110) crystal facets of BiVO<sub>4</sub>, *Nat. Commun.*, 2013, **4**, 1432.
- 138 Z. Pan, V. Nandal, Y. Pihosh, T. Higashi, T. Liu, J. A. Röhr, K. Seki, C. Chu, K. Domen and K. Katayama, Elucidating the Role of Surface Energetics on Charge Separation during Photoelectrochemical Water Splitting, *ACS Catal.*, 2022, **12**, 14727–14734.
- 139 Y. Luo, S. Suzuki, Z. Wang, K. Yubuta, J. J. M. Vequizo, A. Yamakata, H. Shiiba, T. Hisatomi, K. Domen and K. Teshima, Construction of Spatial Charge Separation Facets on BaTaO<sub>2</sub>N Crystals by Flux Growth Approach for Visible-Light-Driven H<sub>2</sub> Production, *ACS Appl. Mater. Interfaces*, 2019, **11**, 22264–22271.